Electronic Supplementary Information (ESI)

Probing the Effects of Ester Functional Group, Alkyl Side Chain Length and Anion on Bulk Nanostructure of Ionic Liquids: A Computational Study

Mostafa Fakhraee, Mohammad Reza Gholami*

Department of Chemistry, Sharif University of Technology,
Tehran, 11365-11155, Iran

(*Corresponding author e-mail: gholami@sharif.edu)

1- A brief review of nanostructure organization in different series of ILs

Several investigations were assigned to the exploration of tail aggregation in liquid phase of various set of ILs as follows:

C. J. Margulis examined the structural and dynamical traits of $[C_nmim][PF_6]$ (n= 6, 8, 10, 12) ILs using MD simulations. It was yielded that couple cation and anion become more structured as the alkyl chain is lengthened.[1]

Y. Wang *et al.* employed MD simulations to investigate the tail aggregation of the $[C_nmim][NO_3]$ family of ILs using multi-scale coarse-graining method. The authors found that elongation of the uncharged domain of tail groups leads to a liquid crystal-like structure which consequently effect on the properties of the ILs.[2] They disclosed that IL with longer alkyl chain of anion (octylsulfate) is more structured. Nanometer-scale structuring in ILs belong to $[C_nmim][PF_6]$ and $[C_nmim][Tf_2N]$ series were inquired by Canongia Lopes and Pádua using an all-atom force field of the AMBER/OPLS_AA family.[3] Conspicuous aggregation of the alkyl chains in non-polar domains is observed for ILs with alkyl side chain length longer than or equal to C_4. Furthermore, The existence of the nanosegregation in polar and non-polar domains was also reported by Pádua *et al.* for simulating $[C_nmim][PF_6]$ (from $[C_2mim][PF_6]$ to $[C_8mim][PF_6]$) family using an all-atom force field.[4] Also, The investigated MD simulation of $[C_nmim][Tf_2N]$ ($[C_1mim][Tf_2N]$, $[C_2mim][Tf_2N]$, $[C_6mim][Tf_2N]$, and $[C_8mim][Tf_2N]$), families by Tsuzuki *et al.* exhibited that the height of center of masses RDFs peaks were slightly enhanced with increasing the alkyl side chain length.[5] Shimizu *et al.* employed MD simulation for investigation of $[CH_3N(C_4H_9)_3][Tf_2N]$, $[CH_3N(C_6H_{13})_3][Tf_2N]$, and $[CH_3N(C_8H_{17})_3][Tf_2N]$ ILs[6] which are earlier studied by using small-angle X-ray scattering.[7] Likewise, similar findings were later reported by Greaves *et al.* for probing the nanostructure of a series of protic ILs (PILs)

containing alkylammonium, dialkylammonium, trialkylammonium, and cyclic ammonium cations paired with organic or inorganic anions by means of the small- and wide angle X-ray scattering (SAXS and WAXS). The segregation of the polar and non-polar components was observed for many selected PILs. This nanostructure ordering of PILs was enhanced for longer alkyl chain.[8]

Besides, Pensado *et al.* studied the influences of the ester functional group in the alkyl side chain of $[C_1COOC_5C_1im][C_8SO_4]$ and $[C_1COOC_5C_1im][Tf_2N]$ ILs on the micro-phase segregation between polar and neutral domains and also the gas solubility in these ILs by use of the atomistic MD simulations.[9] In another work, Triolo *et al.* prepared the extensive experimental evidence of a nano-scale organization in the ILs of the families $[C_nC_1im][Cl]$, $[C_nC_1im][BF_4]$, $[C_nC_1im][PF_6]$, $[C_nC_1im][Tf_2N]$, and $[C_2C_1im][C_nSO_4]$ using X-ray diffraction.[10-14] Moreover, Paredes *et al.* explored the effect of lengthening alkyl side chain of the anion in the bulk phase structure of $[C_2C_1im][C_nSO_4]$ (n=2 to 8) families. This is indeed observed for the shortest side chains, but from $[C_4C_1im][PF_6]$ onward, the trends are reversed.[15] Yeganegi *et al.* studied the structures and dynamics of nine geminal dicationic ILs $C_n(mim)_2X_2$, (n= 3, 6, and 9 and X= PF_6, BF_4, and Br) using MD simulations of all-atom potential model.[16] Shen et al. reported possibility of a third nanostructures region of 11 new protic ionic liquids with fluorous anions (FPILs) resulting from segregation of the polar, uncharged alkyl side and fluorocarbon domains of the these ILs by use of the small- and wide-angle X-ray scattering (SAXS and WAXS) for the first time.[17]

Li *et al.* studied the nano-scale structural arrangement of dicationic ILs (DILs), consisting of $[C_n(mim)_2](X)_2$ (n=3, 6, 9, 12, 16 and X = Br, BF_4, PF_6) and monocationic ILs (MILs) such as $[C_nmim][X]$ (n= 3, 6, 9 and X = Br, BF_4, PF_6) by use of the MD simulations. The different nano-scale structuring in DILs and MILs can be observed from those results. It was justified by the

fact that relatively unfavorable straight and folded linkage models suggested for the nanoaggregates in DILs and the favorable micelle-like organization for those in MILs.[18]

Afterward, Freitas *et al.* emphasized on the heterogeneous families of ILs, such that $[C_3mim][Tf_2N]$, $[(C_1OC_1)mim][Tf_2N]$, $[C_6mim][Tf_2N]$, $[(C_1OC_1)_2mim][Tf_2N]$ were considered for probing the alkyl versus glycol ether chains, $[C_6mim][C_4SO_3]$ and $[N_{4444}][C_4SO_3]$ were simulated for investigation of the effect of mono-versus tetra-alkyl Substituted cations, $[C_4NH_3][Tf_2N]$, $[C_4NH_3][C_1COO]$, $[C_4NH_3][C_8COO]$ protic versus aprotic ILs were chosen to be explored periphery the influences of anions side chain length, and finally focused on the substitution of the anion with the same cation $[C_4mim][Tf_2N]$, $[C_4mim][PF_6]$, $[C_4mim][C_1SO_3]$, and $[C_4mim][C_1COO]$.[19] Comprehensive MD simulation study has been carried out by Shimizu *et al.* in order to complete and extend the structural analysis on the mesoscopic segregation observed in homologous series of ILs, $[C_nC_1im][Tf_2N]$ ($2 \leq n \leq 10$).[20] Nearly at the same time K. Wei *et al.* surveyed the influence effect of different side chain length on the microscopic structure of hydroxyl-functionalized ILs by performing all atom MD simulations for 1-(n-hydroxyalkyl)-3-methylimidazolium nitrate, where n variable from 2 to 12. They concluded that, increasing chain length pushes the both polar and uncharged group to be more ordered and the degree of spatial heterogeneity of those groups obviously enhanced, but -OH group does not significant effect on the degree of spatial heterogeneity owing to the increasing flexibility of cationic side chains. Furthermore, the tight aggregations of non-polar domains are hindered by the addition of –OH group to the cationic tail.[21]

In addition, Hayes *et al.* determined the of cation alkyl chain length and anion type on the PILs, including ethylammonium hydrogen sulfate, ethylammonium formate, ethylammonium thiocyanate and butylammonium thiocyanate using neutron diffraction and computer

simulations.[22] It was founded that elongation of the cation alkyl chain length brings about better segregation between polar and natural regions whilst changing the anion has slight effect on amphiphilic nanostructure domains.

Recently, Hayes *et al.* published a review about structure and nanostructure in ILs in which several related investigations have been summarized.[23]

2. Force field parameters and MD details

Intra- and intermolecular forces between ions were computed by using the following force field equation: [24]

$$
\begin{aligned}
U_{tot} = {} & \sum_{ij}^{bonds} k_{r,ij} \, (r_{ij} - r_{0,ij})^2 + \sum_{ijk}^{angles} k_{\theta,ijk} \, (\theta_{ijk} - \theta_{0,ijk})^2 \\
& + \sum_{ijkl}^{dihedrals} \sum_{m=1}^{4} V_{m,ijkl} \, [1 + (-1)^m \cos(m\varphi_{ijkl})] \\
& + \sum_{ijkl}^{improper} \sum_{m=1}^{4} V_{m,ijkl} \, [1 + (-1)^m \cos(m\varphi_{ijkl})] \\
& + \sum_{i=1}^{N-1} \sum_{j>i}^{N} \left\{ 4\varepsilon_{ij} \left[\left(\frac{\sigma_{ij}}{r_{ij}} \right)^{12} - \left(\frac{\sigma_{ij}}{r_{ij}} \right)^{6} \right] + \frac{1}{4\pi\varepsilon_0} \frac{q_i q_j}{r_{ij}} \right\}
\end{aligned}
\tag{1}
$$

All MD simulations, in present study, were correctly performed by the use of the DL_POLY 2.18 program package.[25] Initially, all selected ILs were optimized at B3LYP/6-311++G(d,p) level of theory using Gaussian package program[26] in the absence of imaginary frequencies. Subsequently, the optimized structures were replicated in three dimensions to create initial configuration of the simulation box. The elimination of surface effects which are attributed to collision of particles to the walls of simulation box was conducted by using periodic boundary conditions. Furthermore, to achieve an actual volume of the simulation box, all executions were carried out in NPT (P =1 atm) of Nosé-Hoover[27] thermostat/barostat ensemble with considering relaxation time 0.1 and 0.5 ps for the thermostat and barostat respectively. Afterward, the total energy and volume of simulation boxes were successfully converged by 1.5 ns production runs with time step 10^{-3} ps at each desired temperatures. Since all simulations are initially started from an equilibrated configuration, this production time can be appropriately suitable. It should be noted that all ensemble averages were calculated over 1.2×10^6 steps. In addition, coordinates and velocities at each time step were incorporated using Verlet leapfrog algorithm.[28] VdW

interactions were sufficiently considered using large radius cut-off 16 Å. Furthermore, the electrostatic interactions take into account with Ewald summation method[29] with a precision of 10^{-6}. Number of ion pairs is summarized in Table S1. In addition, the utilized force field parameters in this work are collocated in Tables S2 to S5.

Table S1. Number of ion pairs in the box of simulation.

ILs	[Br]	[NO$_3$]	[BF$_4$]	[PF$_6$]	[TfO]	[Tf$_2$N]
[C$_1$COOC$_1$C$_1$im]	252	216	216	180	180	150
[C$_1$COOC$_2$C$_1$im]	216	180	180	180	180	125
[C$_1$COOC$_4$C$_1$im]	180	150	150	150	150	125

Table S2. VdWs parameters and point charge of each atom in [C$_1$COOC$_n$C$_1$im] (n= 1, 2, 4) cations

atoms	potential type	q (au)	ε (kJ.mol^{-1})	σ (Å)
C$_2$	LJ	-0.11	0.29288	3.55
C$_{4,5}$	LJ	-0.13	0.29288	3.55
N	LJ	0.15	0.71128	3.25
H$_2$	LJ	0.21	0.12552	2.42
H$_{4,5}$	LJ	0.21	0.12552	2.42
C$_{6,10}$	LJ	-0.17	0.27614	3.50
C$_7$	LJ	0.76	0.43932	3.75
O$_8$	LJ	-0.43	0.87864	2.96
O$_9$	LJ	-0.50	0.71176	3.00
C$_{11}$	LJ	0.30	0.27614	3.50
C$_{12}$	LJ	-0.12	0.27614	3.50
C$_{13}$	LJ	-0.12	0.27614	3.50
C$_{14}$	LJ	-0.18	0.27614	3.50
H$_{6,10}$	LJ	0.13	0.12552	2.50
H$_{11}$	LJ	0.00	0.06276	2.42
H$_{12}$	LJ	0.06	0.12552	2.50
H$_{13}$	LJ	0.06	0.12552	2.50
H$_{14}$	LJ	0.06	0.12552	2.50

Table S3. Equilibrium values of bonds length and their constant in $[C_1COOC_nC_1im]$ (n= 1, 2, 4) cations

Bonds	potential type	r_0 (Å)	k_r (kJ.mol^{-1}. Å^{-2})
C_2–H_2	Harmonic	1.08	2845
$C_{4,5}$–$H_{4,5}$	Harmonic	1.08	2845
$C_{6,10}$–$H_{6,10}$	Harmonic	1.09	2845
C_2–N	Harmonic	1.315	3992
$C_{4,5}$–N	Harmonic	1.378	3574
C_4–C_5	Harmonic	1.341	4352
$C_{6,10}$–N	Harmonic	1.466	2820
C_6–C_7	Harmonic	1.522	2653
C_7–O_8	Harmonic	1.200	4770
C_7–O_9	Harmonic	1.344	1791
O_9–C_{11}	Harmonic	1.437	2678
C_{11}–H_{11}	Harmonic	1.090	2845
C_{11}–C_{12}	Harmonic	1.529	2242
C_{12}–H_{12}	Harmonic	1.090	2845
C_{12}–C_{13}	Harmonic	1.529	2242
C_{13}–H_{13}	Harmonic	1.090	2845
C_{13}–C_{14}	Harmonic	1.529	2242
C_{14}–H_{14}	Harmonic	1.090	2845

Table S4. Equilibrium values of angles and their constants in $[C_1COOC_nC_1im]$ (n= 1, 2, 4) cations

Angles	Potential type	Θ_0 (deg)	k_Θ (kJ.mol^{-1}.rad^{-2})
C_2-N-$C_{4,5}$	Harmonic	108.0	585.8
$C_{6,10}$-N-C_2	Harmonic	126.4	585.8
$C_{6,10}$-N-$C_{4,5}$	Harmonic	125.6	585.8
N-C_2-N	Harmonic	109.8	585.8
H_2-C_2-N	Harmonic	125.1	292.9
$C_{4,5}$-$C_{4,5}$-N	Harmonic	107.1	585.8
$C_{4,5}$-$C_{5,4}$-$H_{5,4}$	Harmonic	130.9	292.9
$H_{4,5}$-$C_{4,5}$-N	Harmonic	122.0	292.9
$H_{6,10}$-$C_{6,10}$-N	Harmonic	110.7	313.8
$H_{6,10}$-$C_{6,10}$-$H_{6,10}$	Harmonic	107.8	276.1
N-C_6-C_7	Harmonic	112.7	500.0
H_6-C_6-C_7	Harmonic	109.5	313.8
C_6-C_7-O_8	Harmonic	125.0	669.0
C_7-O_9-C_{11}	Harmonic	115.0	694.5
O_8-C_7-O_9	Harmonic	125.0	694.5
O_9-C_{11}-H_{11}	Harmonic	109.5	418.4
O_9-C_{11}-C_{12}	Harmonic	109.5	418.4
$H_{11,12,13,14}$-$C_{11,12,13,14}$-$H_{11,12,13,14}$	Harmonic	107.8	276.1
$H_{11,12,13}$-$C_{11,12,13}$-$C_{12,13,14}$	Harmonic	110.7	313.8
$C_{11,12}$-$C_{12,13}$-$C_{13,14}$	Harmonic	112.7	488.3

Table S5. Equilibrium values of dihedral angles and their constants in $[C_1COOC_nC_1im]$ (n= 1, 2, 4) cations

Atoms	Potential type	V_1(kJ.mol^{-1})	V_2(kJ.mol^{-1})	V_3(kJ.mol^{-1})
$C_{6,10}$-N-C_2-N	Cosine 3	0.0000	19.460	0.0000
$C_{6,10}$-N-C_2-H_2	Cosine 3	0.0000	19.460	0.0000
C_2-N-$C_{4,5}$-$C_{5,4}$	Cosine 3	0.0000	12.550	0.0000
C_2-N-$C_{4,5}$-$H_{4,5}$	Cosine 3	0.0000	12.550	0.0000
$C_{6,10}$-N-$C_{4,5}$-$C_{4,5}$	Cosine 3	0.0000	12.550	0.0000
$C_{6,10}$-N-$C_{4,5}$-$H_{4,5}$	Cosine 3	0.0000	12.550	0.0000
N-$C_{4,5}$-$C_{5,4}$-N	Cosine 3	0.0000	44.980	0.0000
$H_{4,5}$-$C_{5,4}$-$C_{4,5}$-N	Cosine 3	0.0000	44.980	0.0000
$H_{4,5}$-C_4-C_5-$H_{5,4}$	Cosine 3	0.0000	44.980	0.0000
$C_{4,5}$-$H_{4,5}$-N-$C_{5,4}$	Cosine 3	0.0000	9.2000	0.0000
C_2-H_2-N-N	Cosine 3	0.0000	9.2000	0.0000
N-$C_{6,10}$-C_2-$C_{4,5}$	Cosine 3	0.0000	8.3700	0.0000
$C_{4,5}$-N-$C_{6,10}$-$H_{6,10}$	Cosine 3	0.0000	0.0000	0.5190
C_2-N-$C_{6,10}$-$H_{6,10}$	Cosine 3	0.0000	0.0000	0.0000
C_2-N-C_6-C_7	Cosine 3	0.0000	0.0000	0.0000
$C_{4,5}$-N-C_6-C_7	Cosine 3	4.1274	0.0000	0.0000
N-C_6-C_7-O_8	Cosine 3	-9.1642	14.1359	1.0771
N-C_6-C_7-O_9	Cosine 3	0.0000	0.0000	-1.4853
H_6-C_6-C_7-O_8	Cosine 3	0.0000	0.0000	0.0000
H_6-C_6-C_7-O_9	Cosine 3	0.0000	0.0000	0.5523
C_6-C_7-O_9-C_{11}	Cosine 3	19.5351	21.4388	0.0000
O_8-C_7-O_9-C_{11}	Cosine 3	0.0000	21.4388	0.0000
C_7-O_9-C_{11}-C_{12}	Cosine 3	-5.1045	-0.5272	1.7656
O_9-C_{11}-C_{12}-C_{13}	Cosine 3	11.4307	-0.9581	2.0292
O_9-C_{11}-C_{12}-H_{12}	Cosine 3	0.0000	0.0000	1.6067
C_{11}-C_{12}-C_{13}-H_{14}	Cosine 3	0.0000	0.0000	1.5313
H_{11}-C_{11}-C_{12}-H_{12}	Cosine 3	0.0000	0.0000	1.3305
H_{12}-C_{12}-C_{13}-H_{13}	Cosine 3	0.0000	0.0000	1.3305
H_{13}-C_{13}-C_{14}-H_{14}	Cosine 3	0.0000	0.0000	1.3305
C_{11}-C_{12}-C_{13}-C_{14}	Cosine 3	7.2800	-0.6569	1.1673

3. Quantum theory of atoms in molecule (QTAIM) analysis
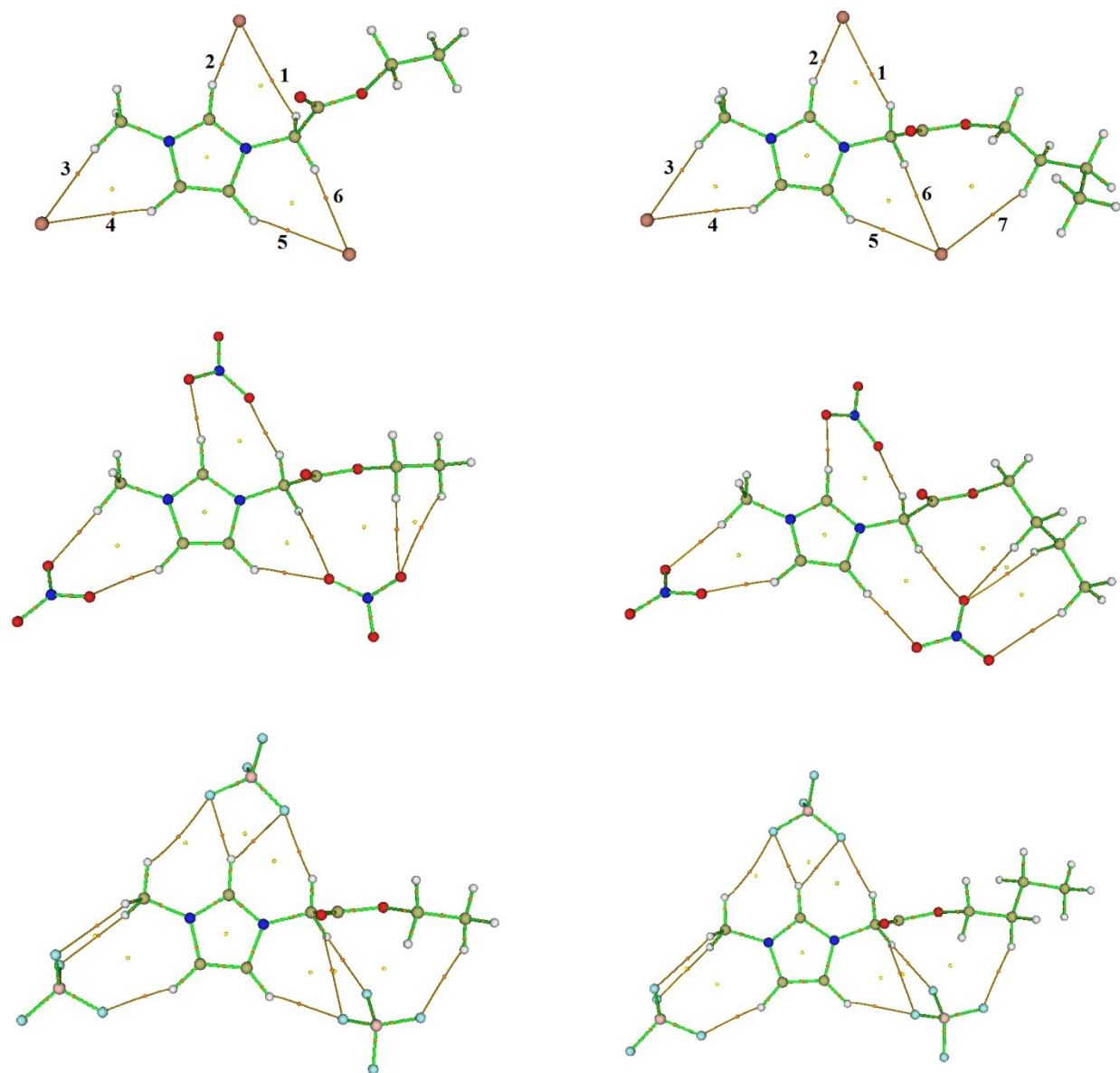
Figure S1. (Online color) BCPs (in orange color), CCPs (in yellow color), and RCPs (in yellow color) of optimized structures for [C$_1$COOC$_{n=2,\ 4}$ C$_1$im][Br]$_3$, [C$_1$COOC$_{n=2,\ 4}$ C$_1$im][NO$_3$]$_3$, [C$_1$COOC$_{n=2,4}$ C$_1$im][BF$_4$]$_3$ ILs, calculated at the B3LYP/6-311++G(d,p) theoretical level.
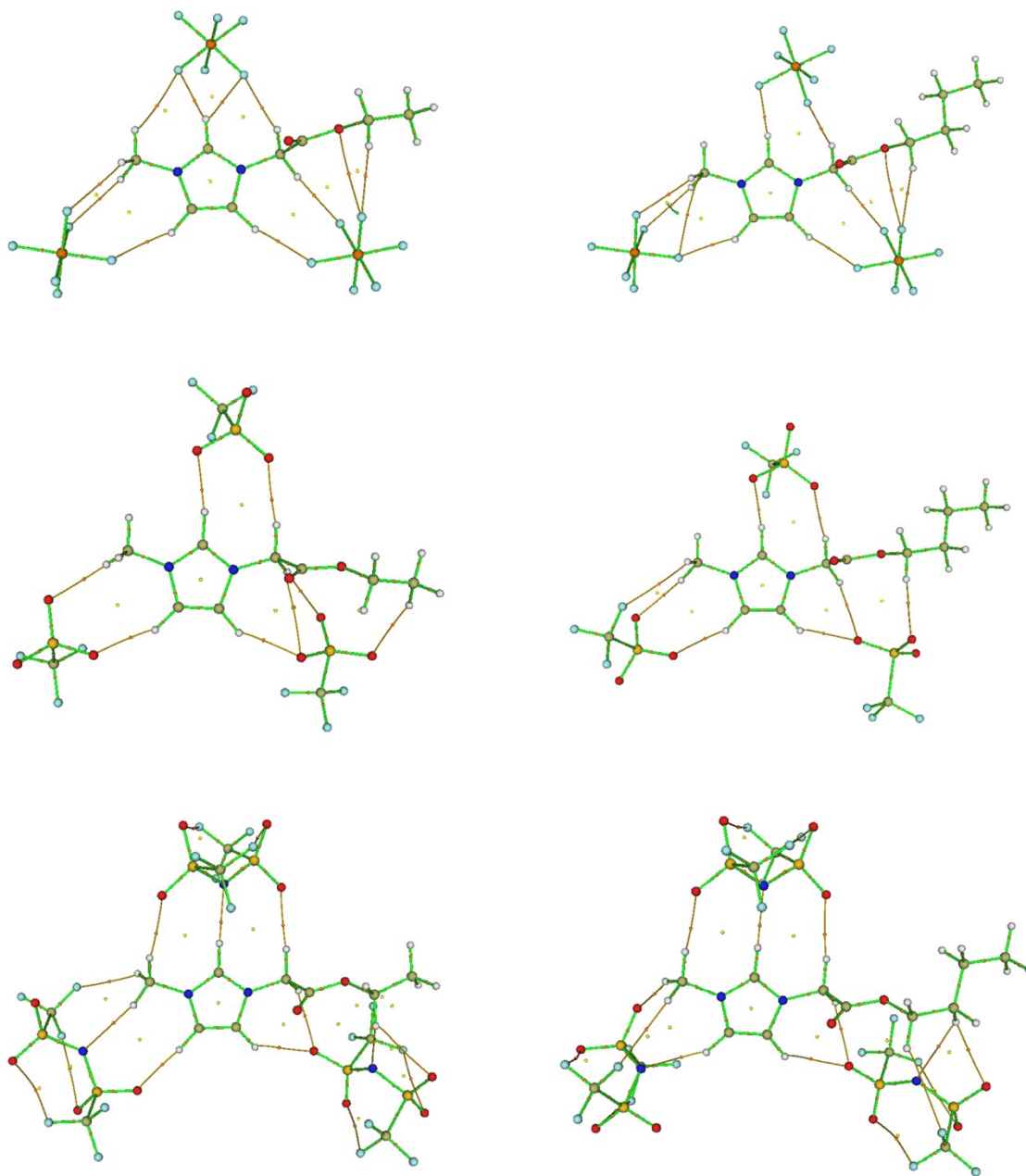
Figure S2. BCPs (in orange color), CCPs (in yellow color), and RCPs (in yellow color) of optimized structures for $[C_1COOC_{n=2, 4} C_1im][PF_6]_3$, $[C_1COOC_{n=2, 4} C_1im][TfO]_3$, $[C_1COOC_{n=2, 4} C_1im][Tf_2N]_3$ ILs, computed at the B3LYP/6-311++G(d,p) level of theory.
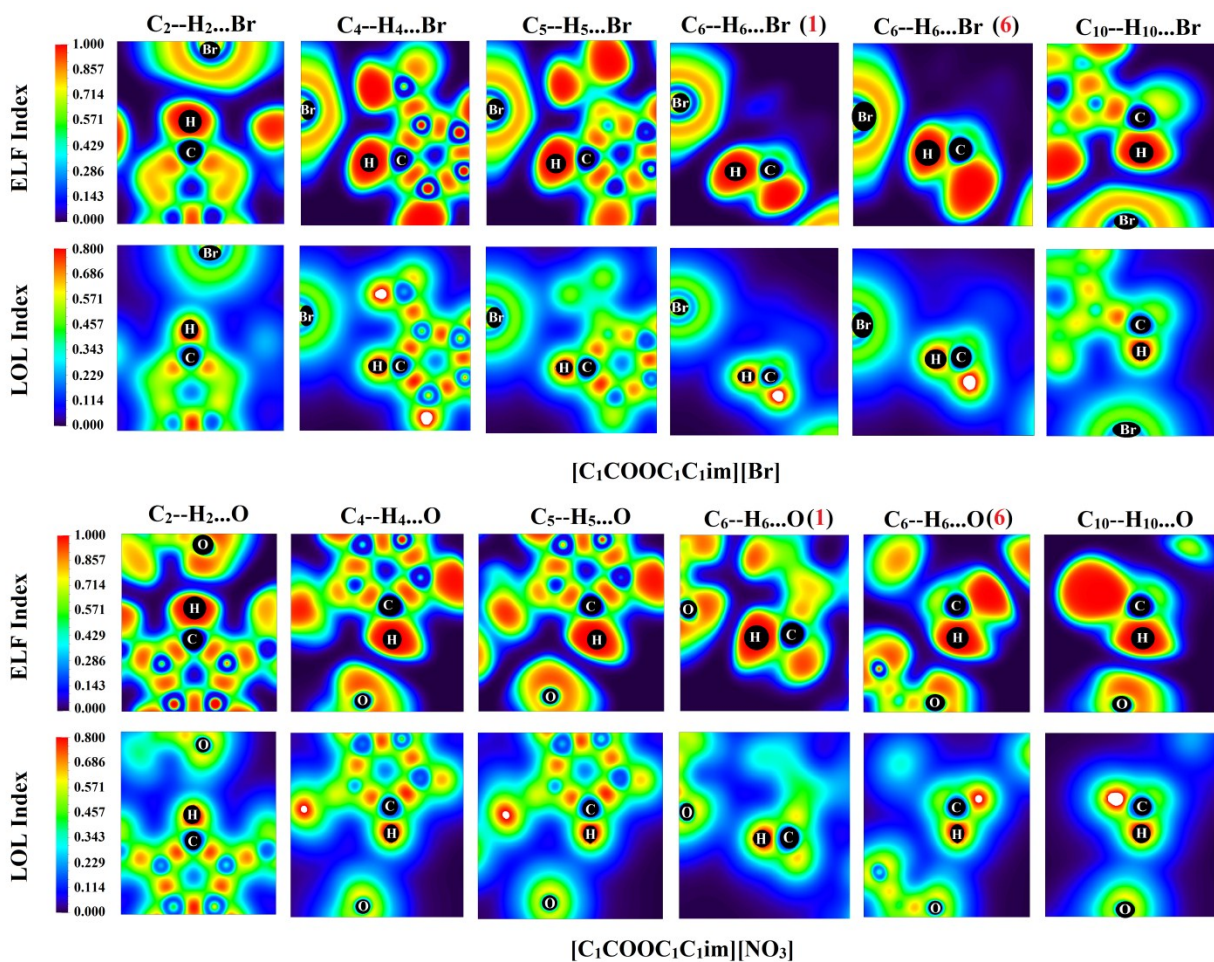
Figure S3. Localized orbital locator (LOL) and electron location function (ELF) models of $[C_1COOC_1C_1im][Br]_3$ and $[C_1COOC_1C_1im][NO_3]_3$ ILs through their BCPs. Indexes correspond to specified labels in figure 2 of the main text.
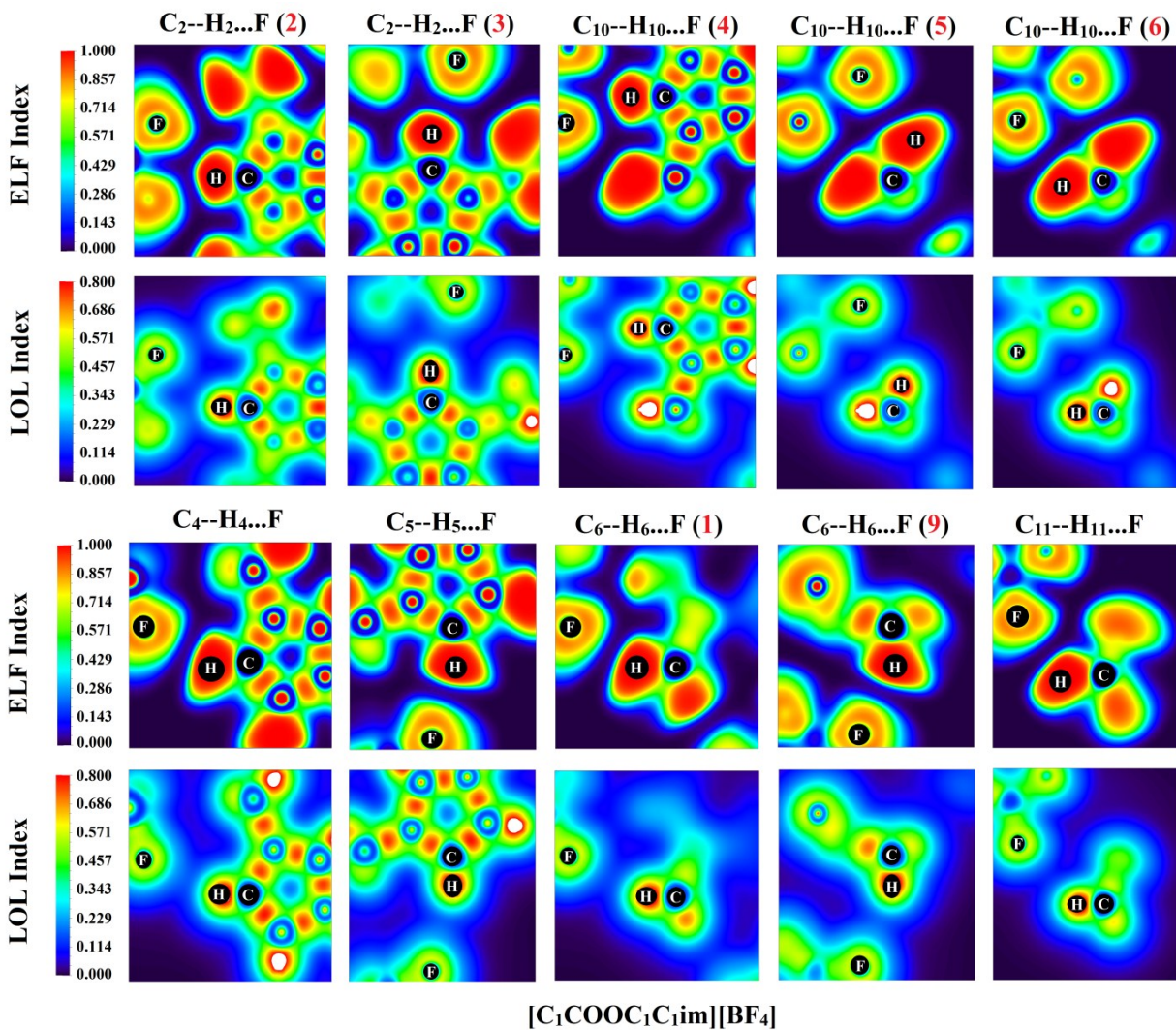
Figure S4. Localized orbital locator (LOL) and electron location function (ELF) models of [C₁COOC₁C₁im][BF₄]₃ IL through their BCPs. Indexes correspond to specified labels in figure 2 of the main text.

Table S6. Topological properties for the interionic interactions at the BCPs of $[C_1COOC_2C_1im][Br]_3$ and $[C_1COOC_2C_1im][Br]_3$ calculated at the B3LYP/6-311++G(d,p) level. Indexes correspond to specified labels in figure S1.

$[C_1COOC_2C_1im][Br]_3$	ρ_b	$\nabla^2\rho_b$	G_b	V_b	$-G_b/V_b$	H_b	ELF	LOL
1	0.00414	0.01076	0.00212	-0.00173	1.22543	0.00039	0.02145	0.12947
2	0.01878	0.04621	0.01035	-0.00919	1.12622	0.00116	0.12286	0.27253
3	0.01369	0.03437	0.00728	-0.00599	1.21536	0.00129	0.08693	0.23604
4	0.00715	0.01769	0.00364	-0.00284	1.28169	0.00080	0.04186	0.17329
5	0.00887	0.02268	0.00466	-0.00377	1.23607	0.00089	0.05195	0.19002
6	0.01448	0.03578	0.00766	-0.00642	1.19315	0.00124	0.09385	0.24371
$[C_1COOC_4C_1im][Br]_3$	ρ_b	$\nabla^2\rho_b$	G_b	V_b	$-G_b/V_b$	H_b	ELF	LOL
1	0.00655	0.01578	0.00329	-0.00263	1.25095	0.00066	0.03825	0.16668
2	0.01917	0.04676	0.01053	-0.00938	1.12260	0.00115	0.12274	0.27241
3	0.01389	0.03491	0.00741	-0.00609	1.21675	0.00132	0.08815	0.23743
4	0.00706	0.01729	0.00356	-0.00279	1.27599	0.00077	0.04086	0.17148
5	0.00790	0.01978	0.00406	-0.00317	1.28076	0.00089	0.04675	0.18167
6	0.00887	0.02279	0.00475	-0.00380	1.25000	0.00095	0.05002	0.18696

4. Electrostatic potential map (ESP)
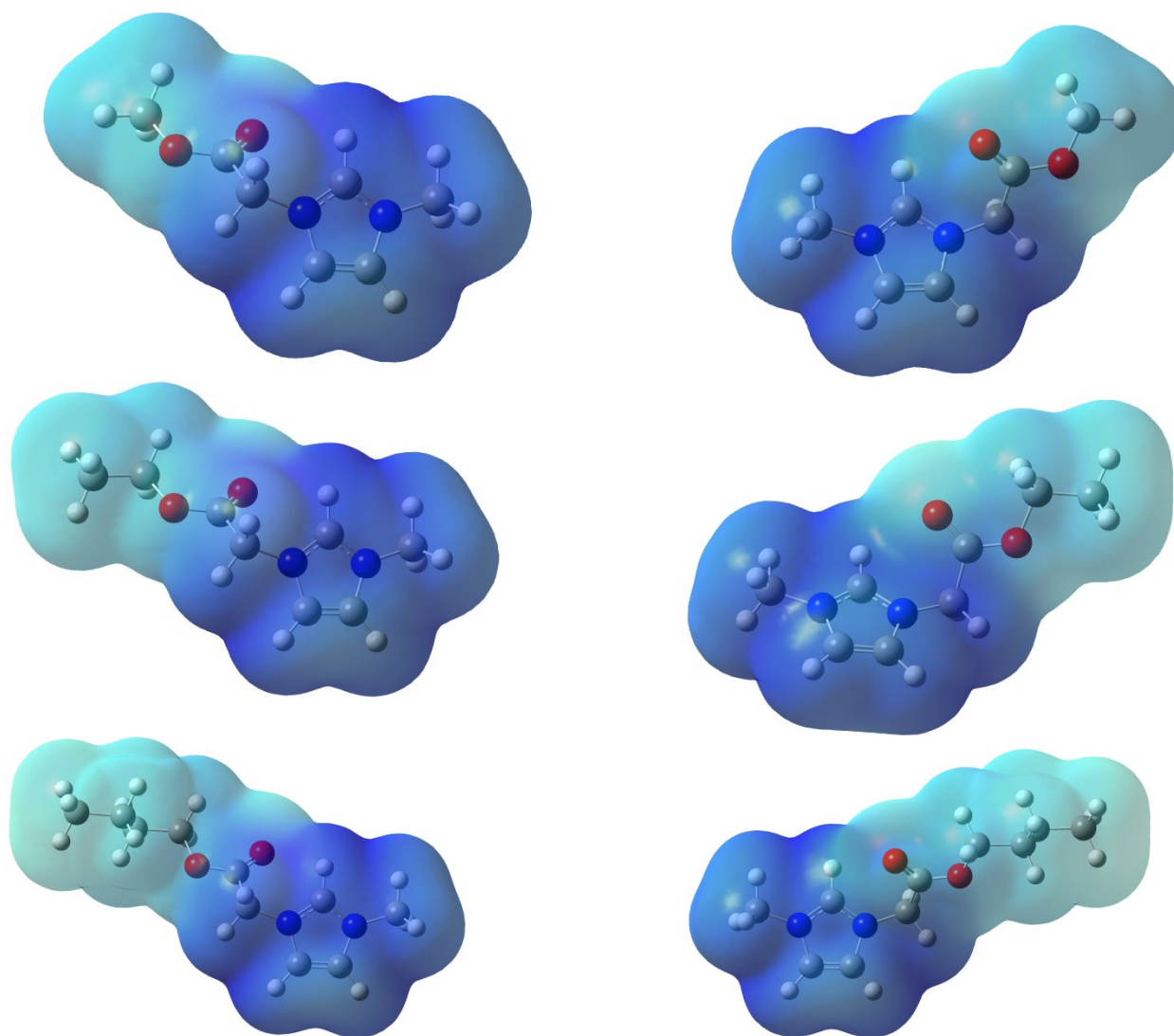
Figure S5. Electrostatic potential map (ESP) of $[C_1COOC_nC_1im]$ cations from two different points of view at the B3LYP/6-311++G(d,p) level. In the ESP surface, blue color is the area with the lowest negative charge, and regions with the high negative charge are determined with red color.
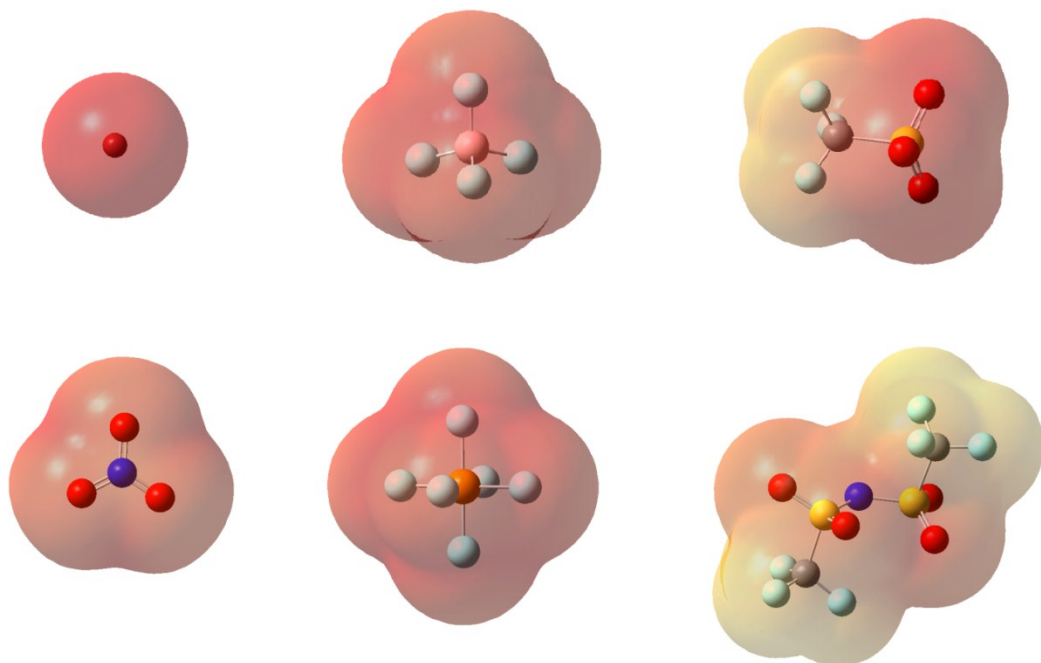
Figure S6. Electrostatic potential map (ESP) of selected anions in the present work at the B3LYP/6-311++G(d,p) level. In the ESP surface, blue color is the region with the lowest negative charge and area with the high negative charge are determined with red color.

5. Radial distribution functions (RDFs)

5.1. Cation-anion site-site RDFs
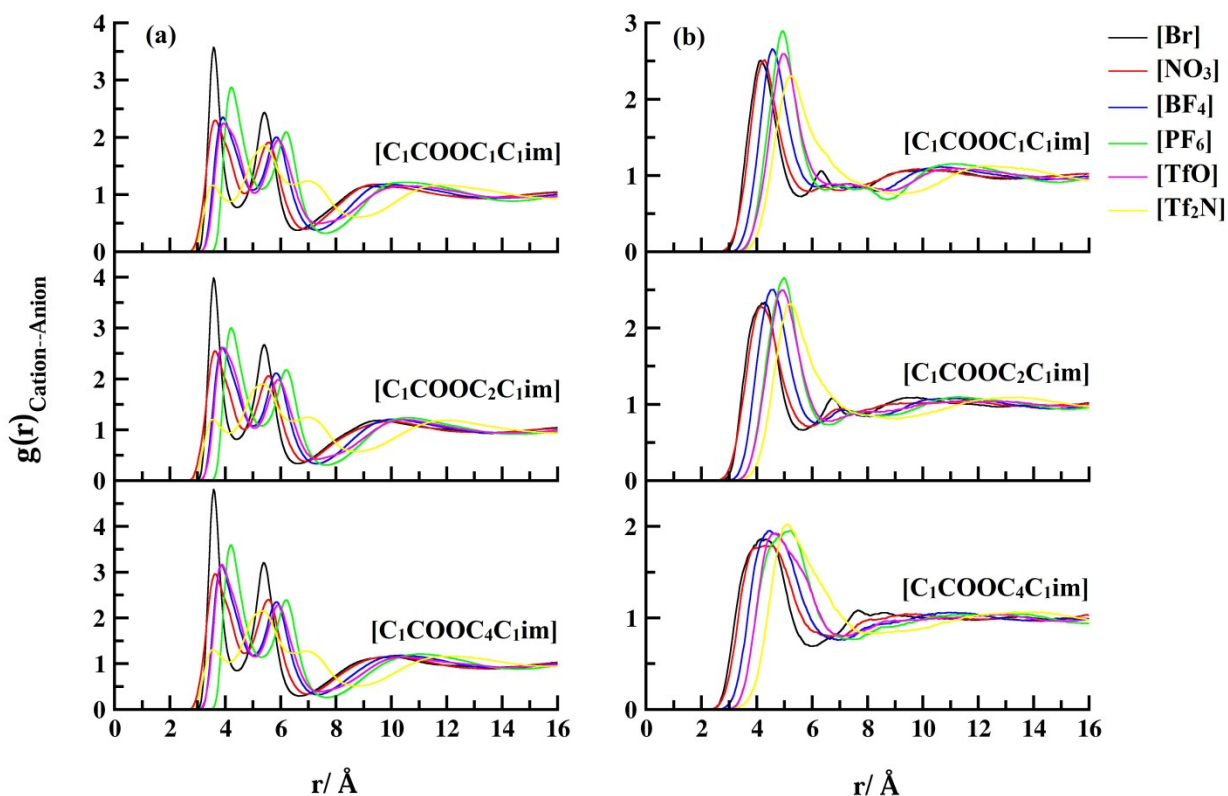
Figure S7. (a) Site-site cation-anion RDFs of C_2 atoms of $[C_1COOC_nC_1im]^+$ (n= 1, 2, 4) cations and nearest atoms to the center of mass anions (N atom for $[NO_3]$ and $[Tf_2N]$, S atom for $[TfO]$, B atom for $[BF_4]$, and P atom for $[PF_6]$) at 400 K. (b) Center of mass cation-anion RDFs of selected ILs.
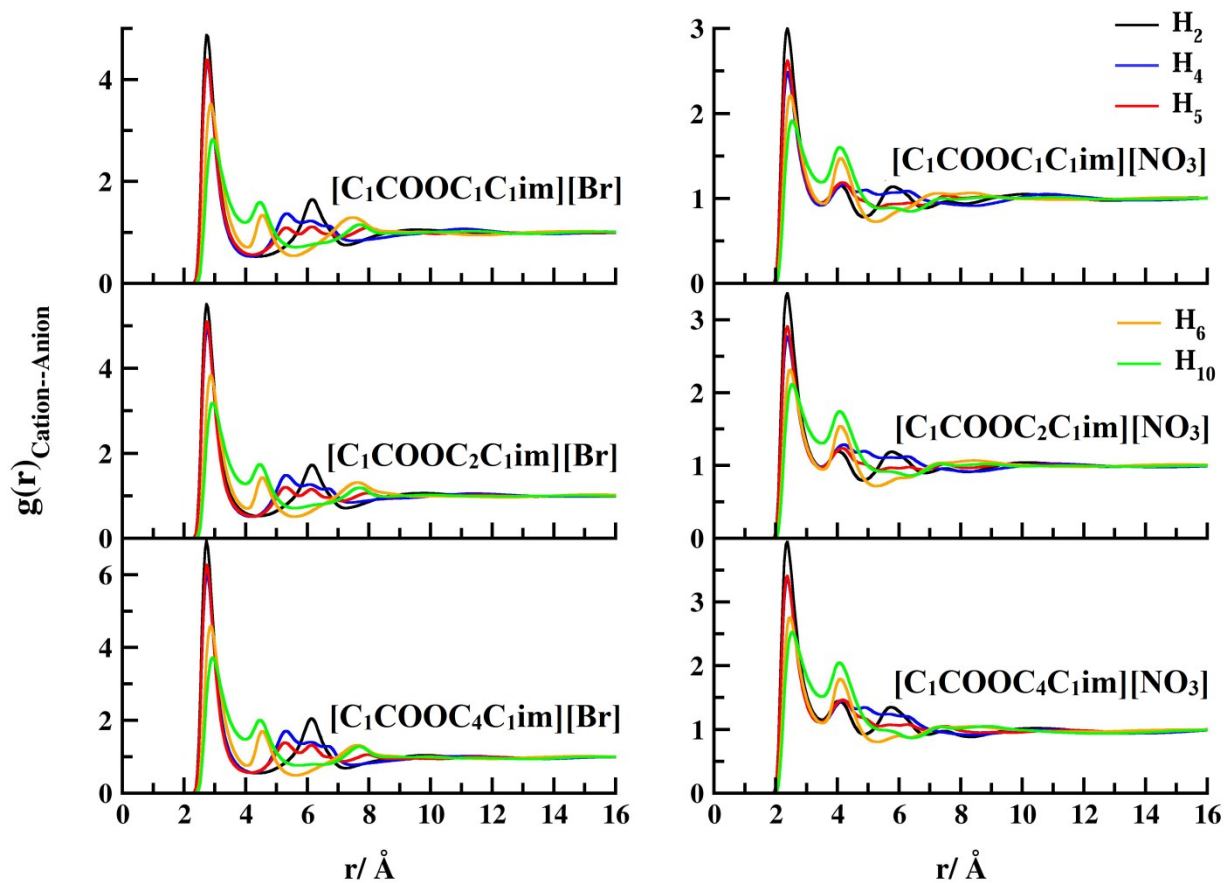
Figure S8. (Online color) H_n-anion RDFs of $[C_1COOC_nC_1im]^+$ (n= 1, 2, 4) cations paired with [Br] and [NO_3] anions at 400 K.
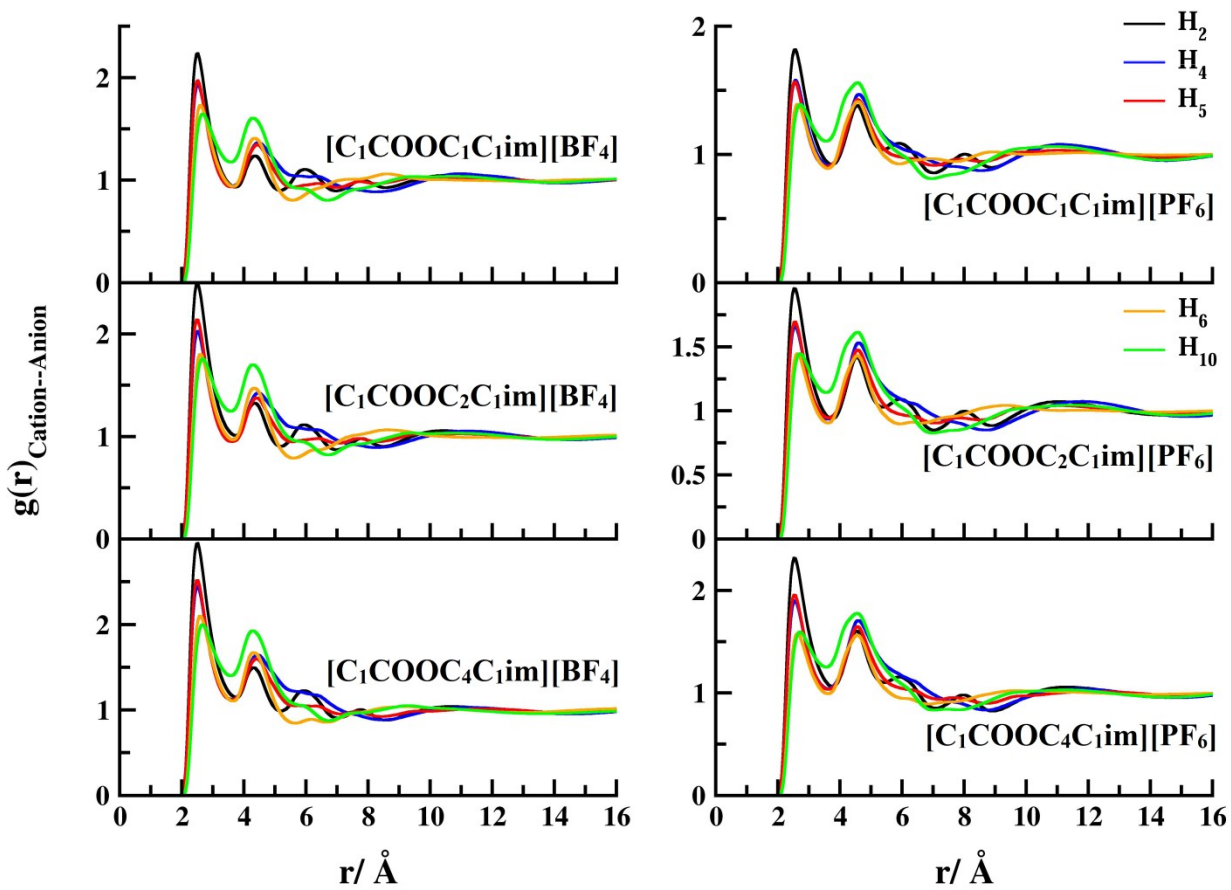
Figure S9. (Online color) H_n-anion RDFs of $[C_1COOC_nC_1im]^+$ (n= 1, 2, 4) cations paired with $[BF_4]$ and $[PF_6]$ anions at 400 K.
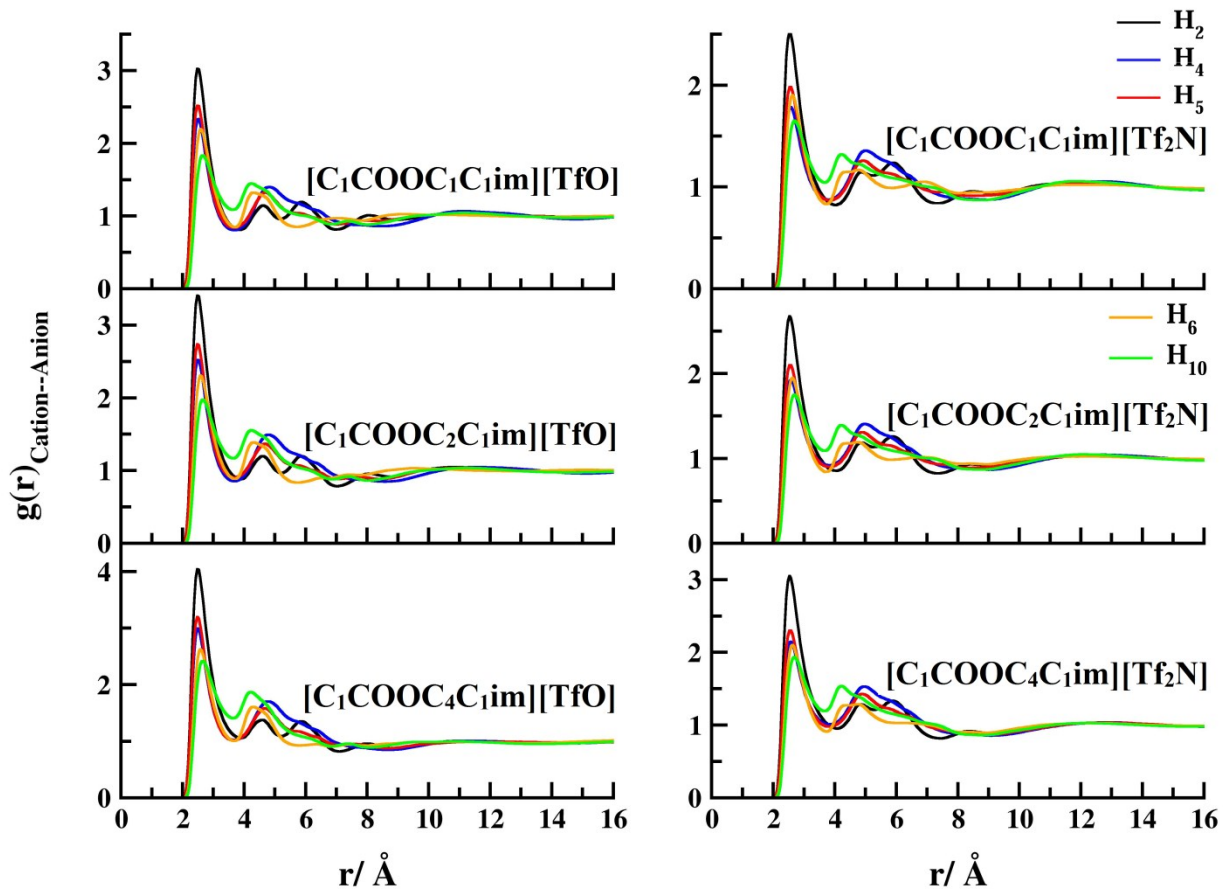
Figure S10. (Online color) H_n-anion RDFs of $[C_1COOC_nC_1im]^+$ (n= 1, 2, 4) cations paired with [TfO] and [Tf$_2$N] anions at 400 K.

Fig. S11 shows the site-site RDFs between C_n (n=11, 12, 13) sites of [$C_1COOC_4C_1$im] ILs and nearest atoms to the center of masses of anions. The nearest atoms to the center of masses of anions were selected, in that, N atom for [NO_3] and [Tf_2N], S atom for [TfO], B atom for [BF_4], and P atom for [PF_6]. From Fig. S11 (a), it can be seen that the height of C_7-anion (n=11, 12, 14) RDF peaks slightly increased with elongation of the alkyl side chain length. The smaller and wider C_7-anion RDF peaks are attributed to cations mated with voluminous anions such as [Tf_2N], whilst the higher probability of finding an anion in the vicinity of the ester function group at closer distances can be found for the other smaller anions. To be more precise, C_7-anion RDF peaks of ILs composed of [Br] have three successive shoulder, highlighting long correlation between their ions. It may be caused from less steric hindrance of this anion which can get close to C_7 as a polar site, efficiently. The maximum probability of C_7-anion RDF peaks for various anions are slightly occurred in different distances based on the size of anions. Fig. S11 (b) represents the site-site RDFs of end carbon atoms of cations and nearest atoms to the center of mass of an anion. The correlation between C_n and anions is gradually diminished with lengthening alkyl side linkage. This is more pronounced for smaller anions with localized negative charge and less steric hindrance.
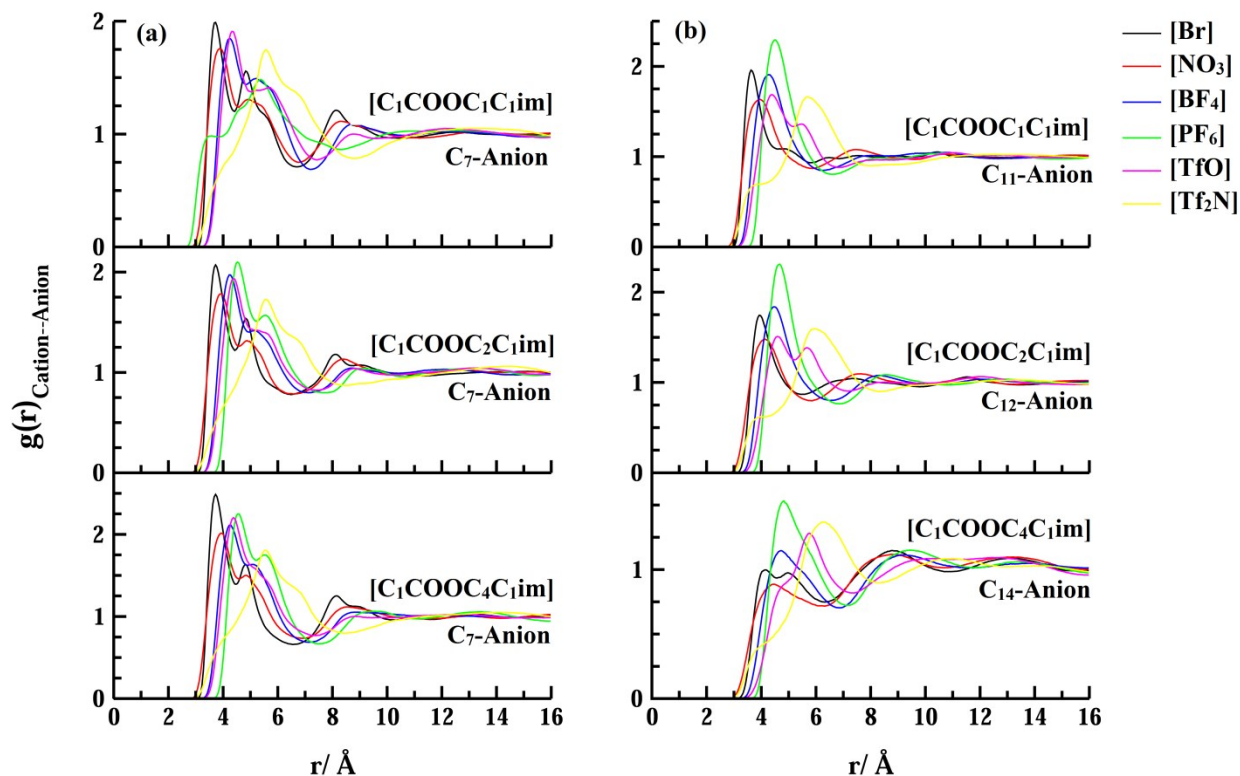
Figure S11. (Online color) (a) Site-site cation-anion RDFs of C_7 site of $[C_1COOC_nC_1im]^+$ (n= 1, 2, 4) cations and nearest atoms to the center of mass anions (N atom for $[NO_3]$ and $[Tf_2N]$, S atom for $[TfO]$, B atom for $[BF_4]$, and P atom for $[PF_6]$) at 400 K. (b) Site-site cation-anion RDFs of terminal atoms (C_n) of $[C_1COOC_nC_1im]^+$ (n= 1, 2, 4) cations and nearest atoms to the center of mass anions (N atom for $[NO_3]$ and $[Tf_2N]$, S atom for $[TfO]$, B atom for $[BF_4]$, and P atom for $[PF_6]$) at 400 K.

Fig. S12 demonstrates the site-site RDFs between C_n (n=11, 12, 13) sites of [$C_1COOC_4C_1im$] ILs and nearest atoms to the center of masses of anions. The cation-anion correlation becomes weaker as a C atom of alkyl linkage located at farther distances from polar domains of cation, suggesting more segregation between charged and uncharged domains for longer alkyl chain. It is more conspicuous for smaller anions.
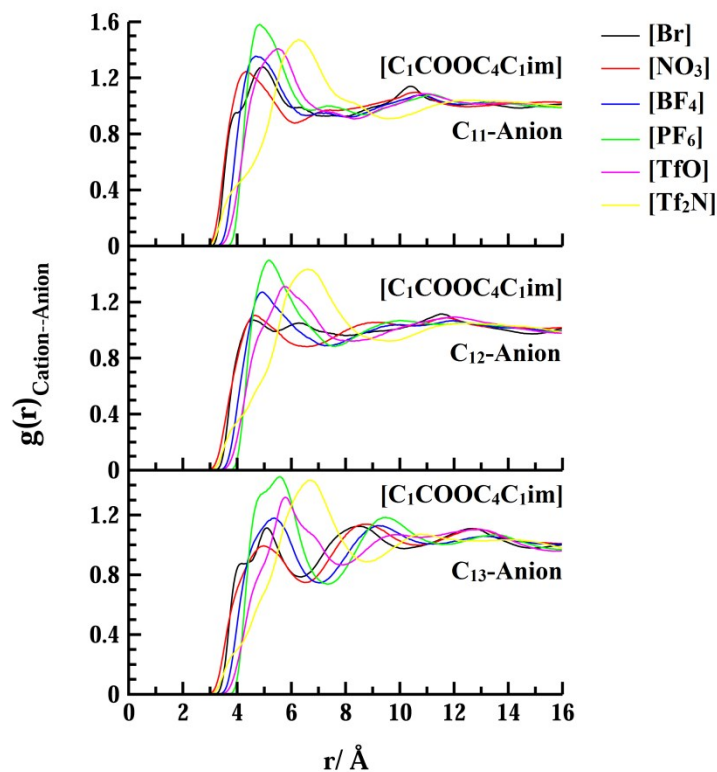
Figure S12. (Online color) Site-site cation-anion RDFs of C_{11}, C_{12}, and C_{13} sites of [$C_1COOC_4C_1im$]$^+$ cation and nearest atoms to the center of mass anions (N atom for [NO_3] and [Tf_2N], S atom for [TfO], B atom for [BF_4], and P atom for [PF_6]) at 400 K.

5.2. Cation-cation site-site RDFs
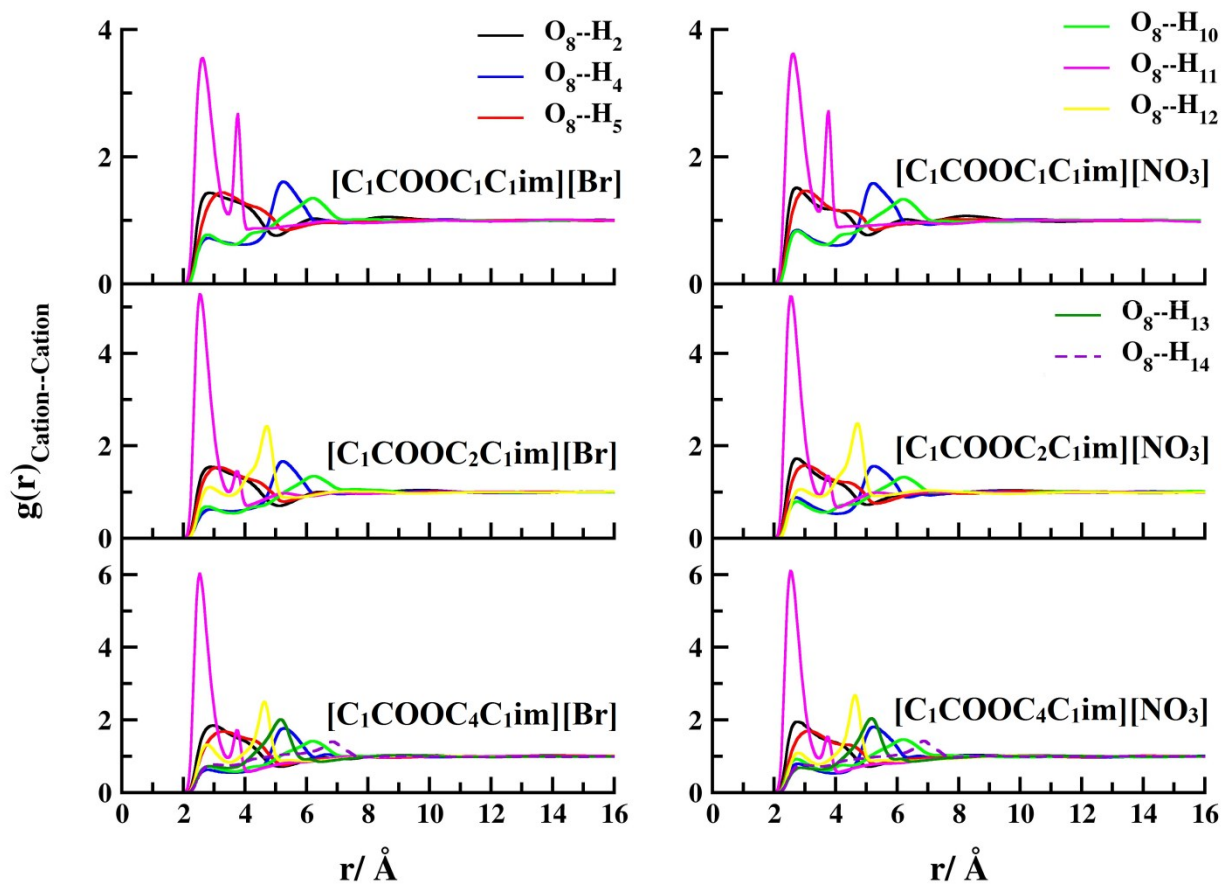
Figure S13. O_8-H_n RDFs of $[C_1COOC_nC_1im][Br]$ and $[C_1COOC_nC_1im][NO_3]$ ILs at 400 K. Indexes correspond to specified labels in figure 1 of the main text.
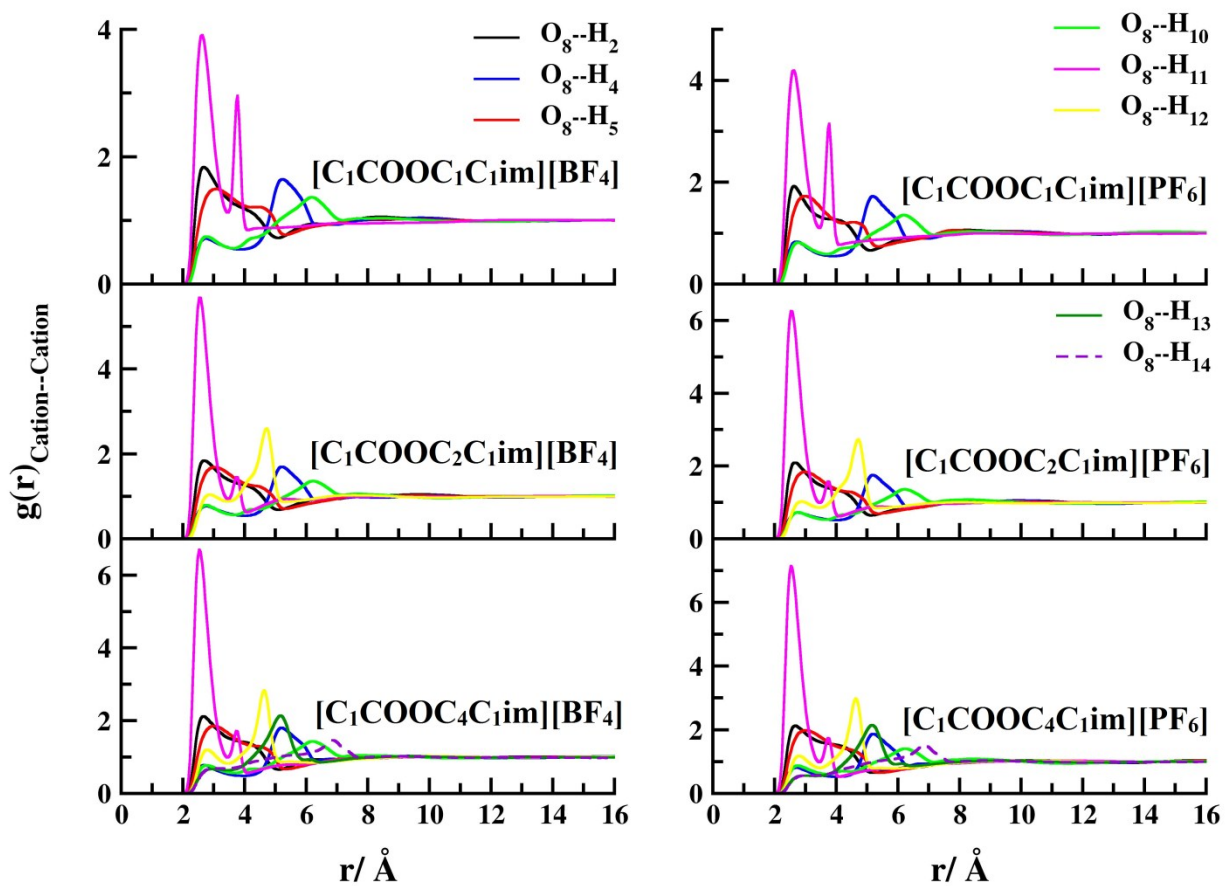
Figure S14. O_8-H_n RDFs of $[C_1COOC_nC_1im][BF_4]$ and $[C_1COOC_nC_1im][PF_6]$ ILs at 400 K. Indexes correspond to specified labels in figure 1 of the main text.
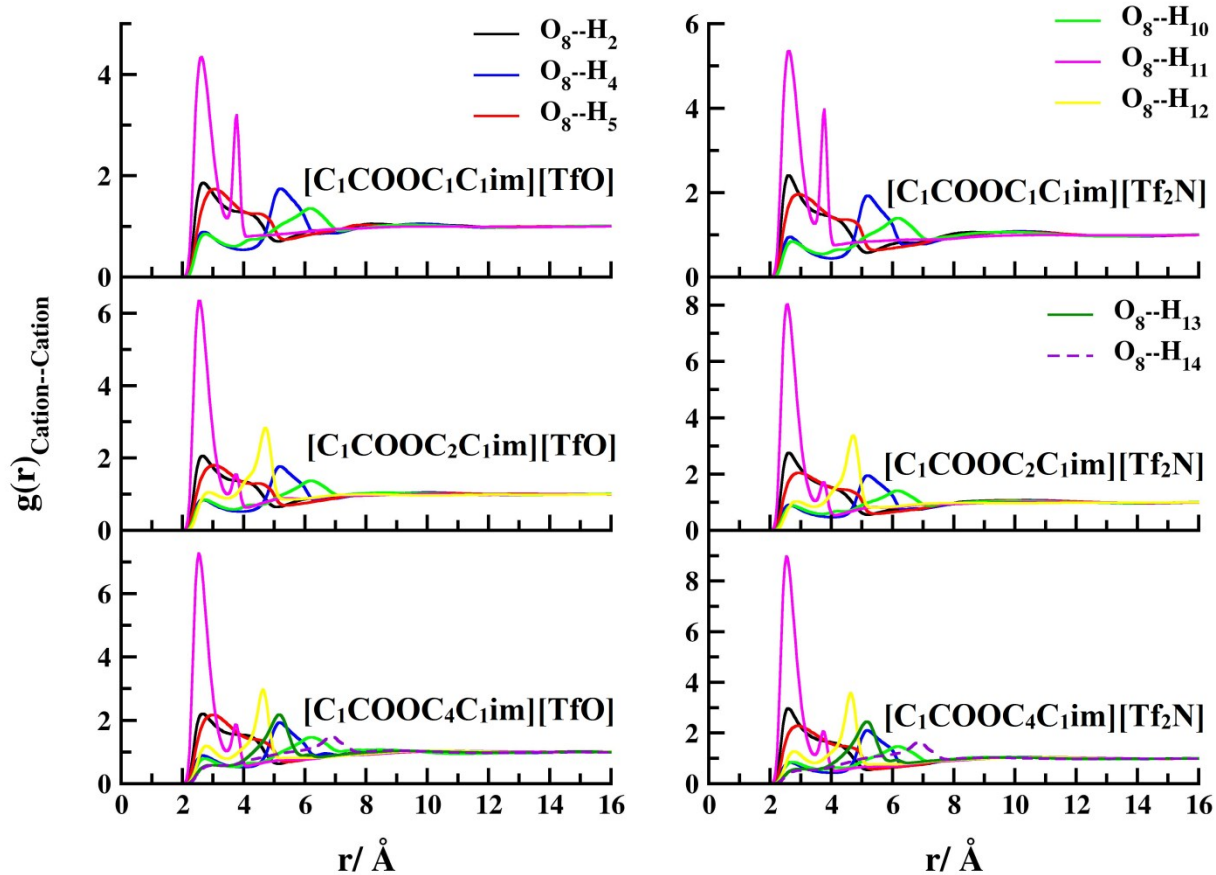
Figure S15. O_8-H_n RDFs of $[C_1COOC_nC_1im][TfO]$ and $[C_1COOC_nC_1im][Tf_2N]$ ILs at 400 K. Indexes correspond to specified labels in figure 1 of the main text.
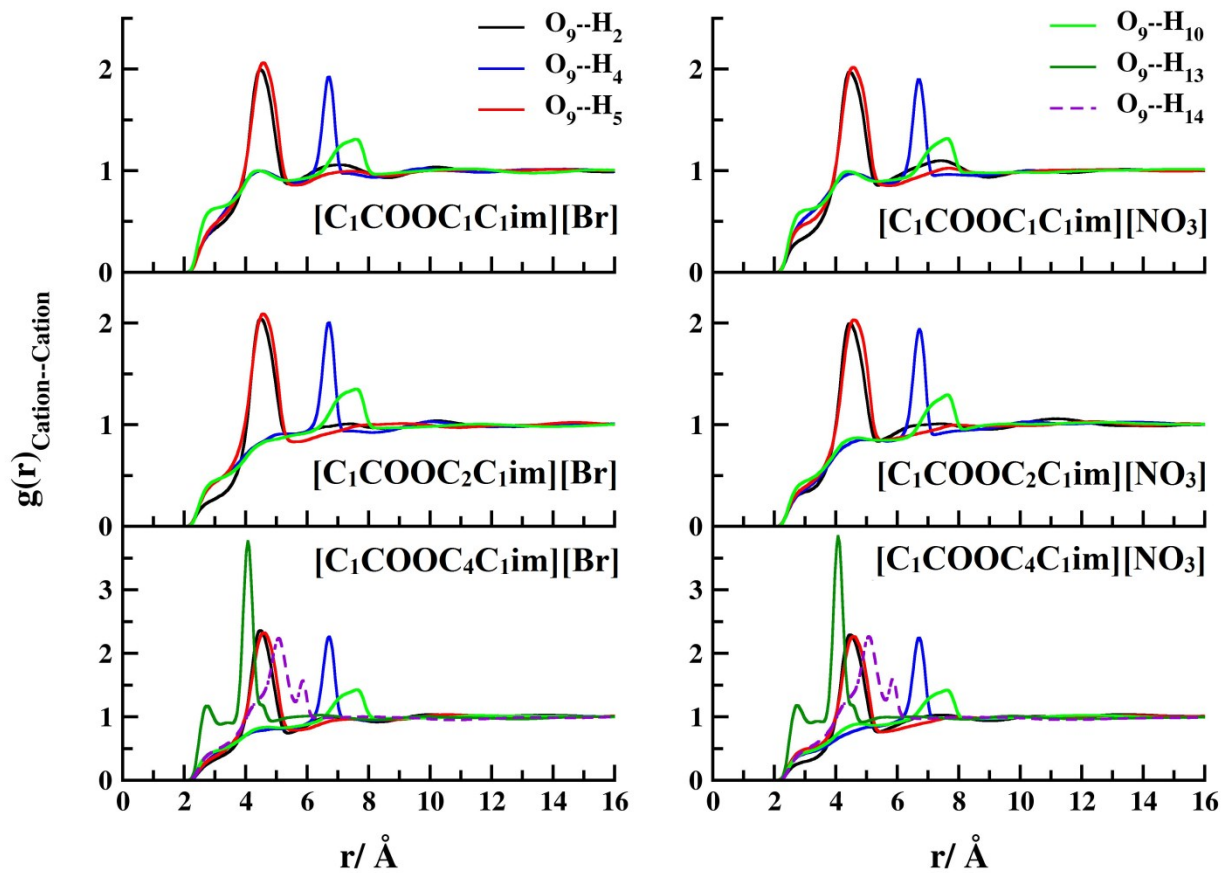
Figure S16. O_9-H_n RDFs of $[C_1COOC_nC_1im][Br]$ and $[C_1COOC_nC_1im][NO_3]$ ILs at 400 K. Indexes correspond to specified labels in figure 1 of the main text.
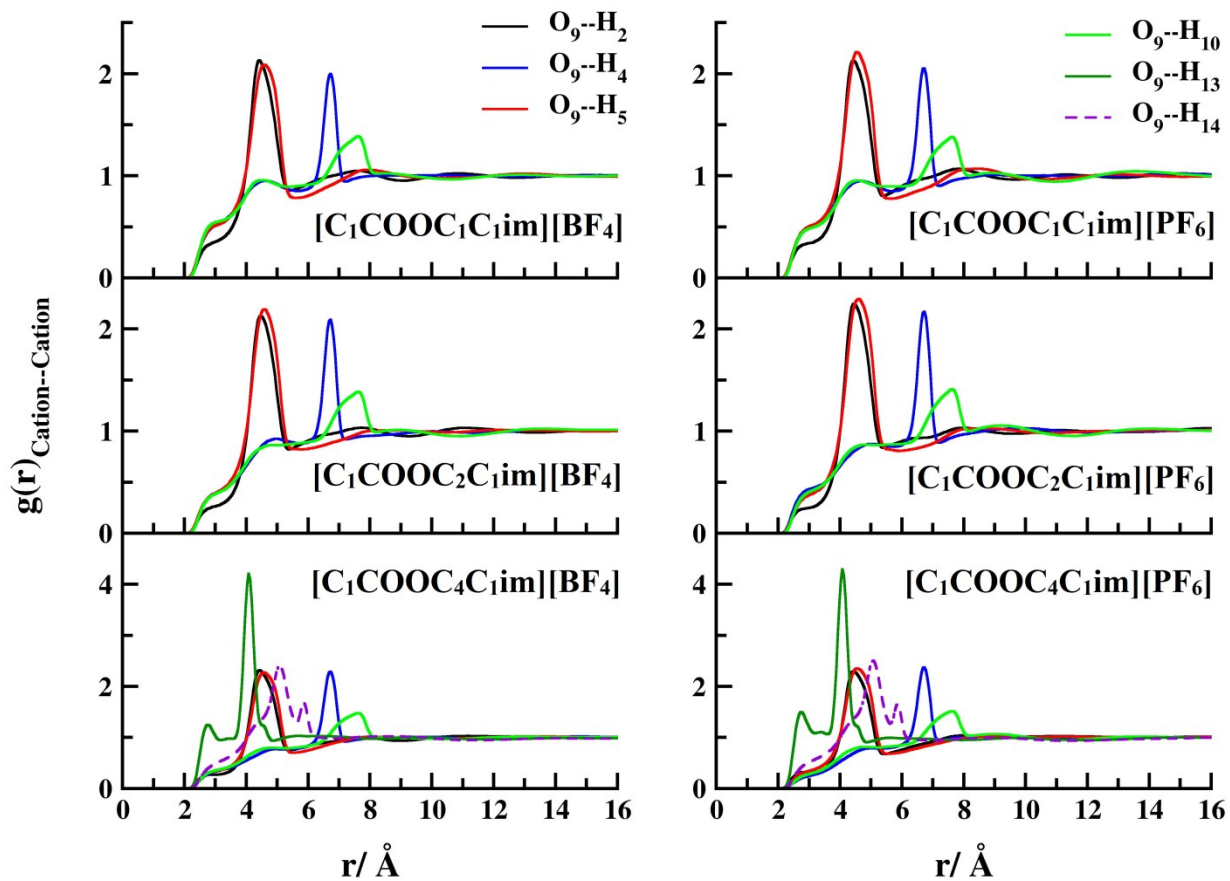
Figure S17. O_9-H_n RDFs of $[C_1COOC_nC_1im][BF_4]$ and $[C_1COOC_nC_1im][PF_6]$ ILs at 400 K. Indexes correspond to specified labels in figure 1 of the main text.
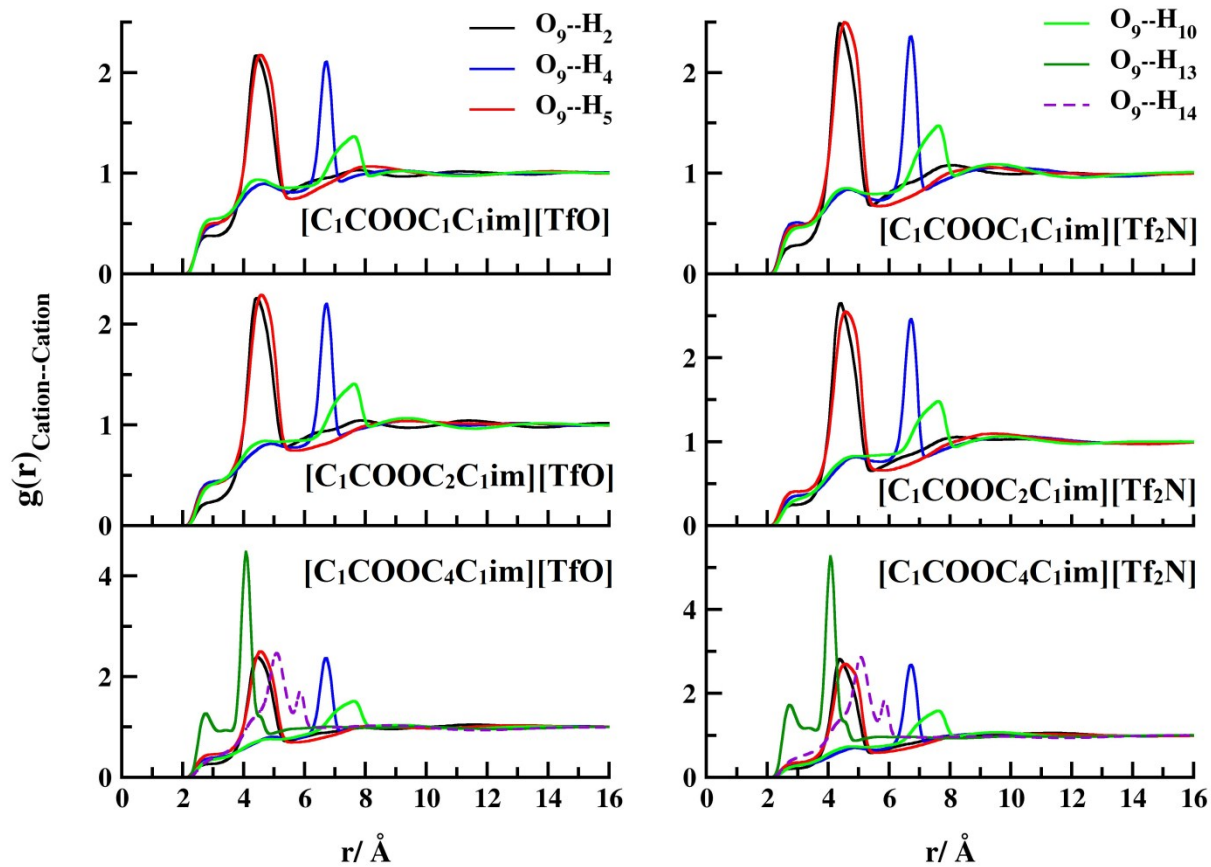
Figure S18. O_9-H_n RDFs of $[C_1COOC_nC_1im][TfO]$ and $[C_1COOC_nC_1im][Tf_2N]$ ILs at 400 K.

Indexes correspond to specified labels in figure 1 of the main text.
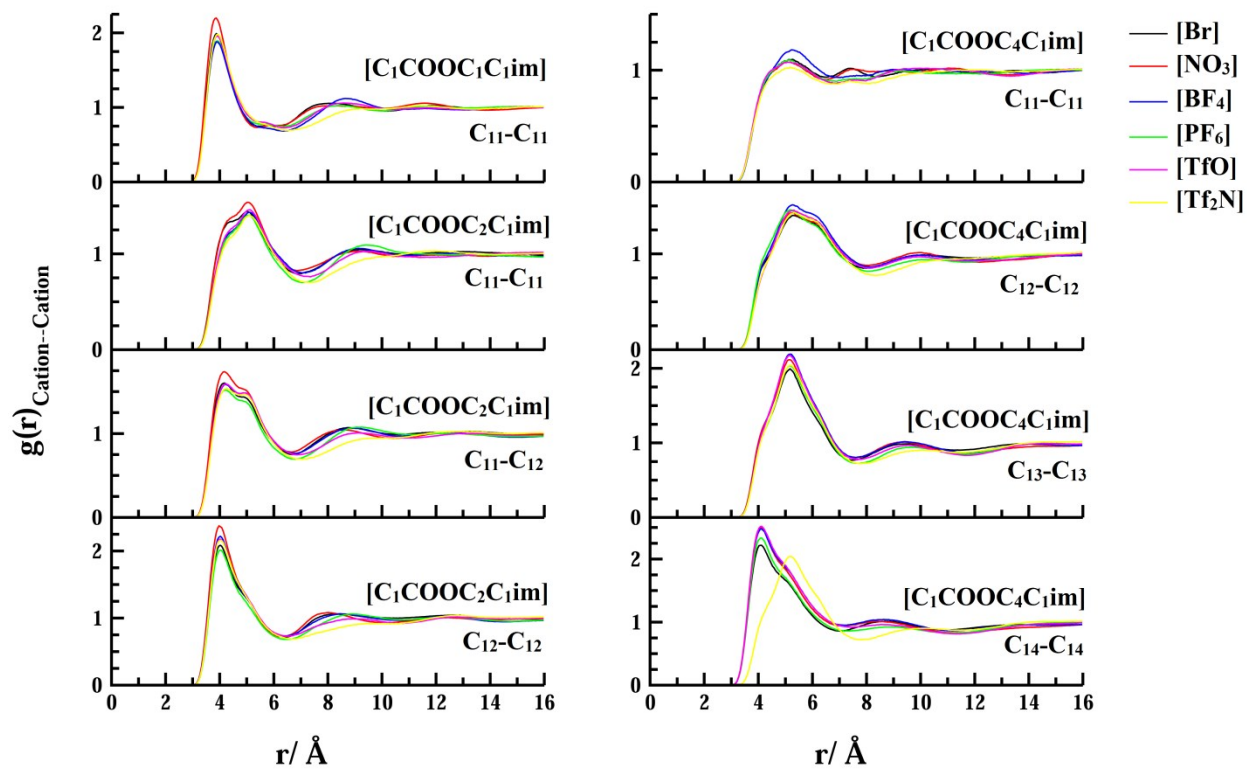
Figure S19. Site-site cation-cation RDFs between the terminal carbon atoms of the alkyl side chain (C_n-C_n) of [$C_1COOC_nC_1im$] cations at 400 K.
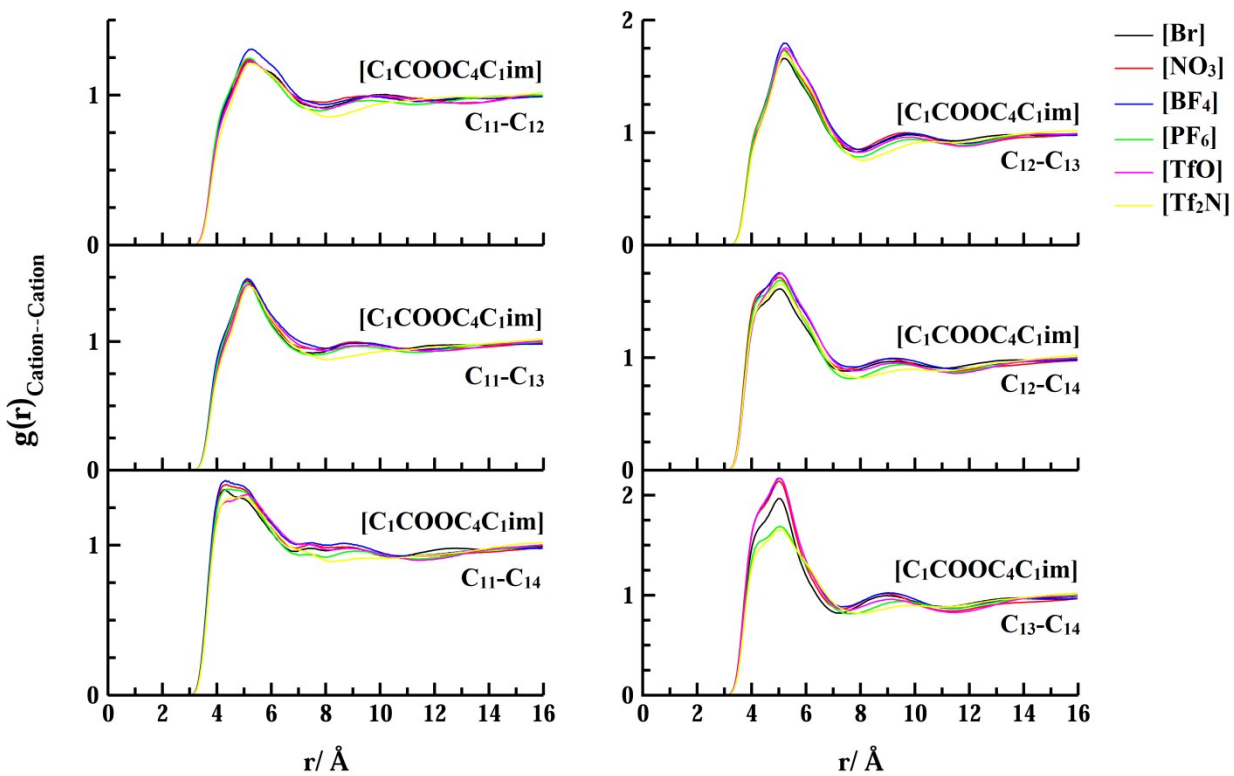
Figure S20. Site-site RDFs between unlike carbon atoms of alkyl side chain of $[C_1COOC_4C_1im]$ cation. Indexes correspond to specified labels in figure 1 of the main text.
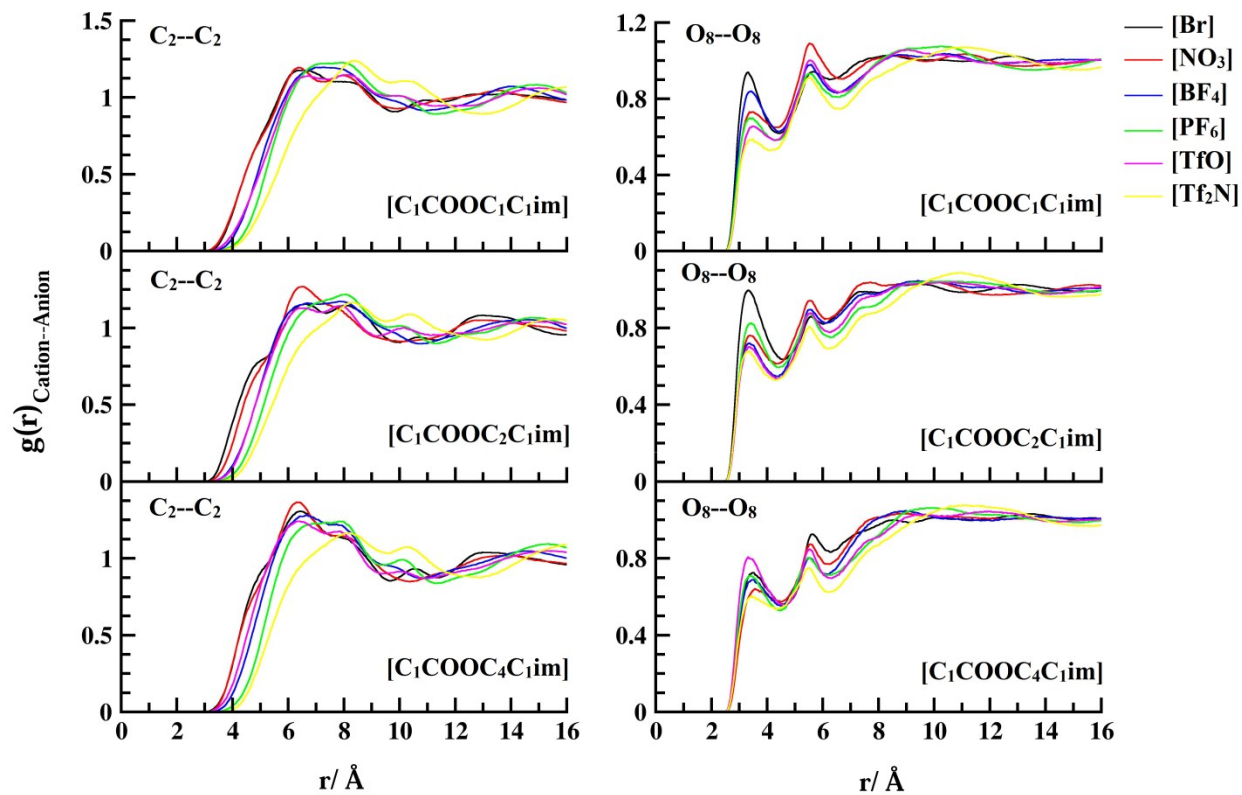
Figure S21. C_2-C_2 and O_8-O_8 RDFs of selected ILs at 400 K. Indexes correspond to specified labels in figure 1 of the main text.

5.3. Anion-anion RDFs

The near atom to the center of mass of an anion was selected for surveying site-site anion-anion RDFs. According to Fig. S17, peaks become slightly sharper for longer alkyl side chain. These RDFs are started at ~4 Å for the smallest anion ([Br]) and move toward farther distances for larger anions. The site-site RDFs of anions indicate very broad peaks in which their first peak placed at around 6-8 Å and the second one at larger distances (~14 Å). To be more precise, the first peak constituted from two or more sequential peaks, distinctively for smaller anions. Actually, voluminous anions, especially [Tf$_2$N] show much broader peaks and their maximum shifted to the farther distances (~8 Å).
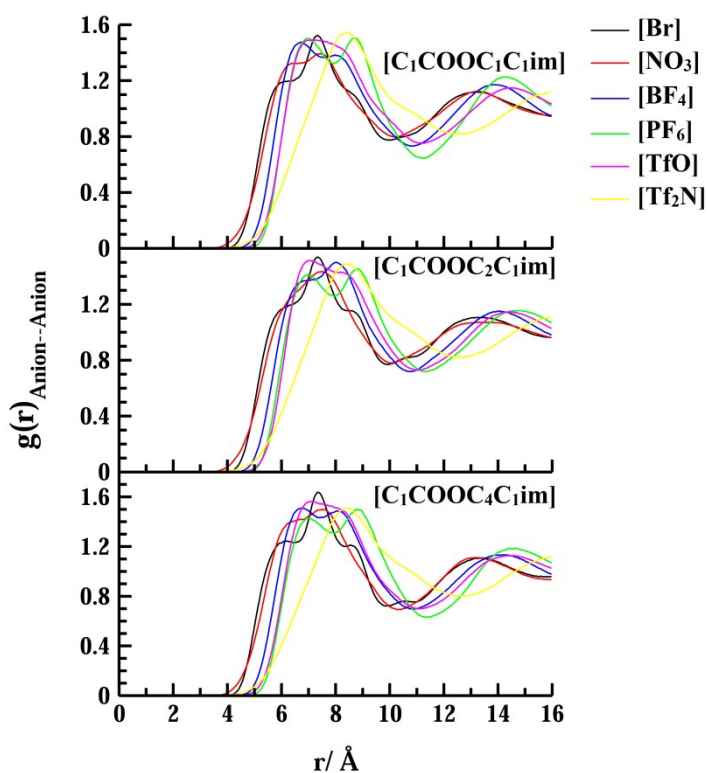
Figure S22. (Online color) Site-site anion-anion RDFs between the nearest atoms to the center of mass of anions (N atom for [NO$_3$] and [Tf$_2$N], S atom for [TfO], B atom for [BF$_4$], and P atom for [PF$_6$]) at 400 K.

6. Spatial distribution functions (SDFs)

6.1. Cation-anion SDFs

Additional structural features of target ILs can be precisely gained by visualizing the tridimensional spatial distribution functions (SDFs). Figs. S23 to S25 show the probability of finding anions around their cations at nine times the average density by means of the TRAVIS package.[30] As it can be observed, anions mainly reside at the top and bottom of the imidazolium-ring, which interact with H_2, H_4, H_5, H_6, and H_{10} at the same time. The weakening direct interionic interactions of H_2-anion can be inferred from the SDFs results, which were already verified by the achieved results of QTAIM. This can be attributed to the strong intra- and intermolecular H bonds between O_8-H_2 sites as well as placing in the vicinity of H_6 site. The thickness of the isosurfaces is bulkier for ILs composed of smaller anions such as [Br] and [NO$_3$], whilst gradually becomes narrower for weakly coordinating anions such as [Tf$_2$N]. The selected anions tend to positioning mostly towards H_6 site rather than to H_{10} atom, which is previously verified by the QTAIM analysis, and cation-anion RDFs. The presence of ester group noticeably enhanced the acidity of H_6 site in comparison with conventional hydrocarbon side chain. With a closer look, there is a slight propensity for anions to associate with H_4 site in comparison with H_5 site. It may be caused by constituting O_8-H_5 intra-molecular hydrogen bonding. Briefly, the existence of the ester group in the alkyl side chain, as a second polar region, brings about competitive cation-anion and cation-cation interactions. Alternatively, a significant modification of the ions arrangement pattern can be observed in comparison to the conventional imidazolium-based ILs.

[C₁COOC₁C₁im][Br]

[C₁COOC₂C₁im][Br]

[C₁COOC₄C₁im][Br]

[C₁COOC₁C₁im][NO₃]

[C₁COOC₂C₁im][NO₃]

[C₁COOC₄C₁im][NO₃]
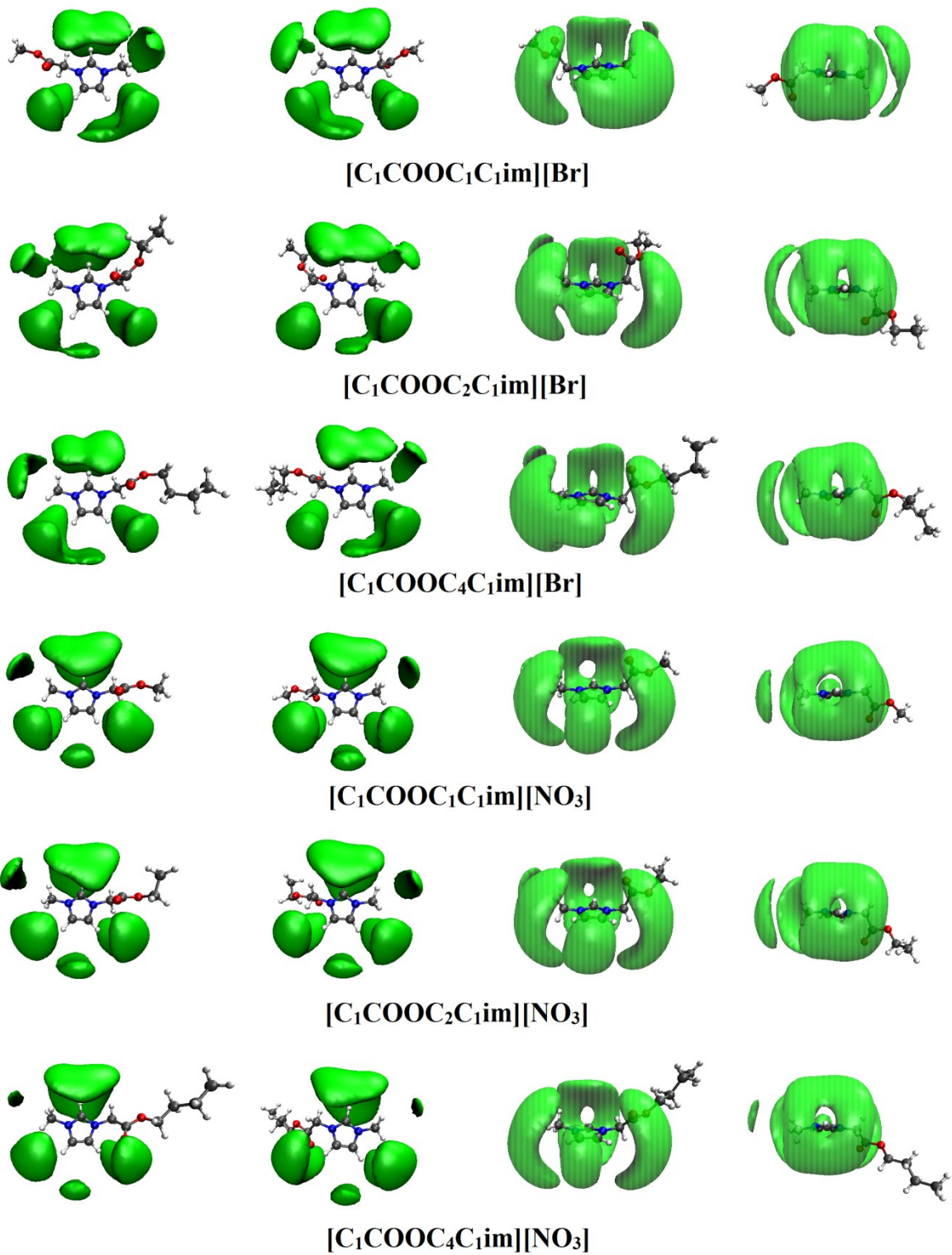
Figure S23. Cation-anion SDFs of [Br] and [NO₃] anions around the imidazolium ring for [C₁COOC$_n$C₁im] (n= 1, 2, 4) cations at 400 K.
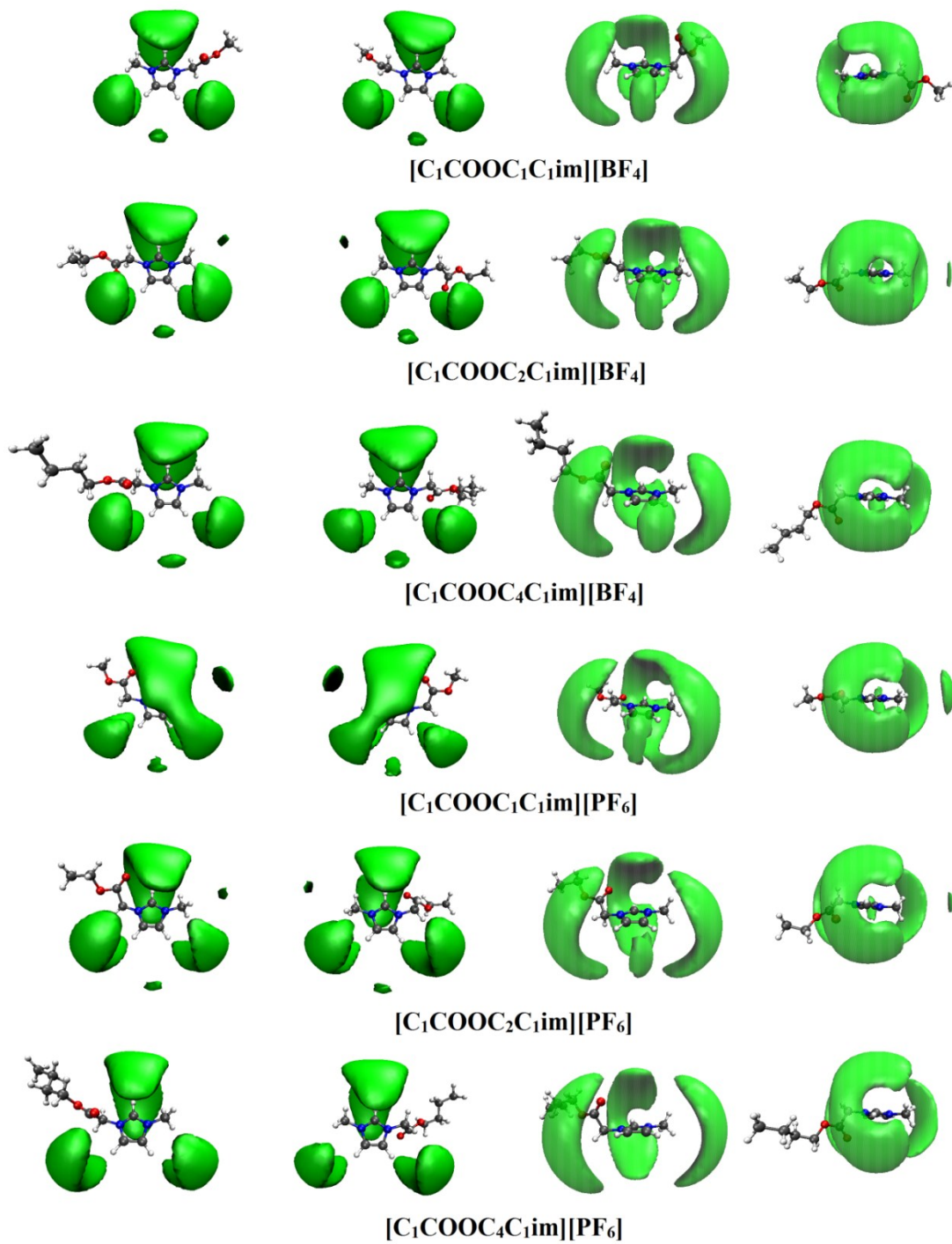
Figure S24. Cation-anion SDFs of [BF_4] and [PF_6] anions around the imidazolium ring for [$C_1COOC_nC_1im$] (n= 1, 2, 4) cations at 400 K.

[C₁COOC₁C₁im][TfO]

[C₁COOC₂C₁im][TfO]

[C₁COOC₄C₁im][TfO]

[C₁COOC₁C₁im][Tf₂N]

[C₁COOC₂C₁im][Tf₂N]

[C₁COOC₄C₁im][Tf₂N]
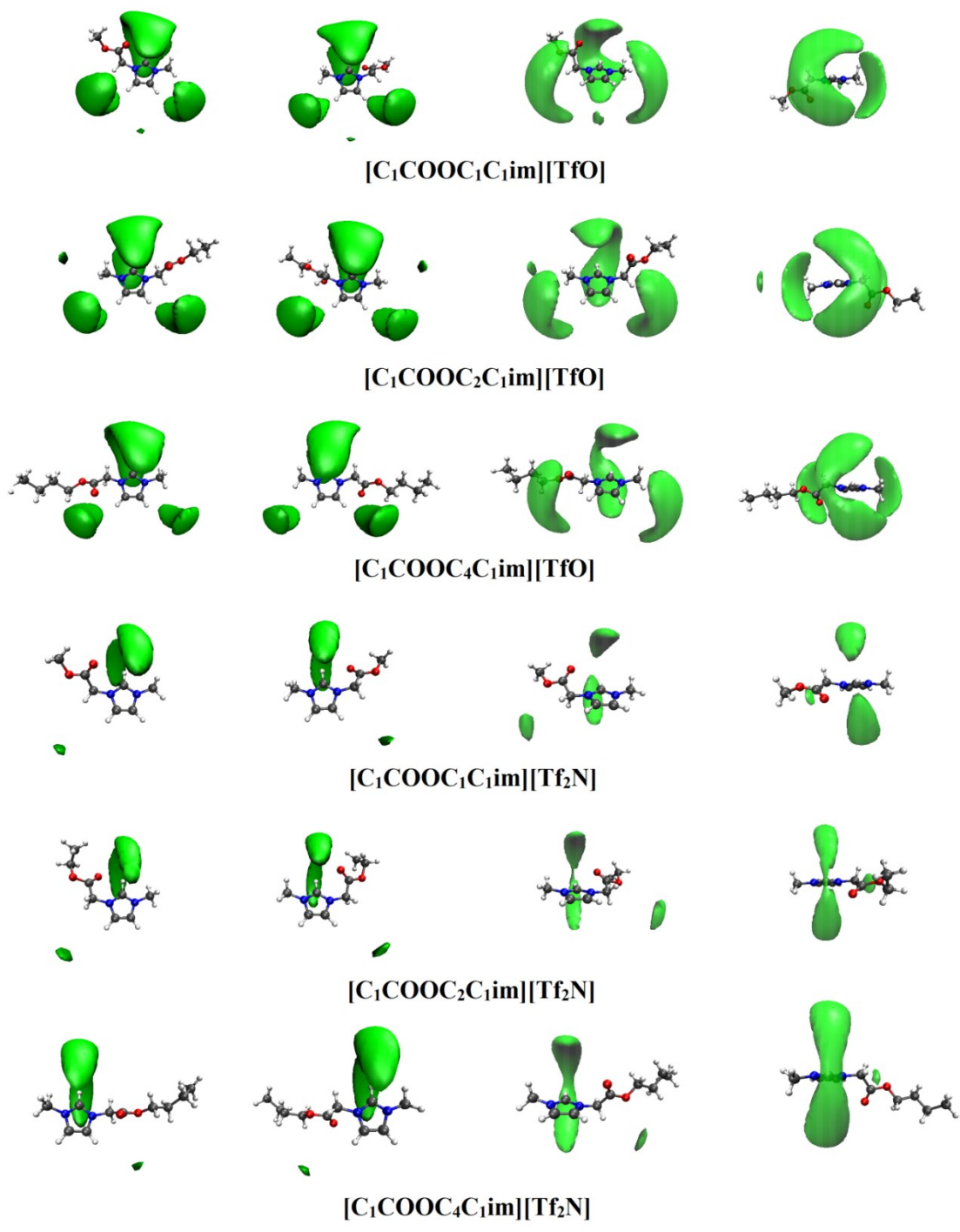
Figure S25. Cation-anion SDFs of [TfO] and [Tf₂N] anions around the imidazolium ring for [C₁COOC$_n$C₁im] (n= 1, 2, 4) cations at 400 K.

6.2. Cation-cation SDFs

More insights into the detailed of cation-cation organization pattern were qualitatively attained by visualizing the cation-cation SDFs, which give the probability of finding neighboring cations around their references cations. Calculated cation-cation SDFs selected ILs are depicted in Figs. S26 to S31. These isosurfaces were drawn four times the average density. It can be understood that neighbor cations mainly located at above and below the imidazolium-ring, highlighting the intra- and intermolecular interaction between ester group and H atoms of the imidazolium-ring. Neighboring cations preferentially positioned at the top of H_2 and H_5 sites. To be more precise, minor elimination of the matching interactions can be found for H_4 site with a profound regard into the cation-cation SDFs. Sensitivity of the aforementioned SDFs to the type of cation can be seen, especially for bulkier anions. The highest cation-cation cohesion is ascribed to the larger cation mixed with the voluminous anions, as earlier proved by the caion-cation RDFs. The possibility of detecting neighbor cations around alkyl side chain of the central cation increased as the alkyl chain is elongated. This is found to be in good agreement with cation-cation RDFs results.

[C₁COOC₁C₁im][Br]

[C₁COOC₂C₁im][Br]
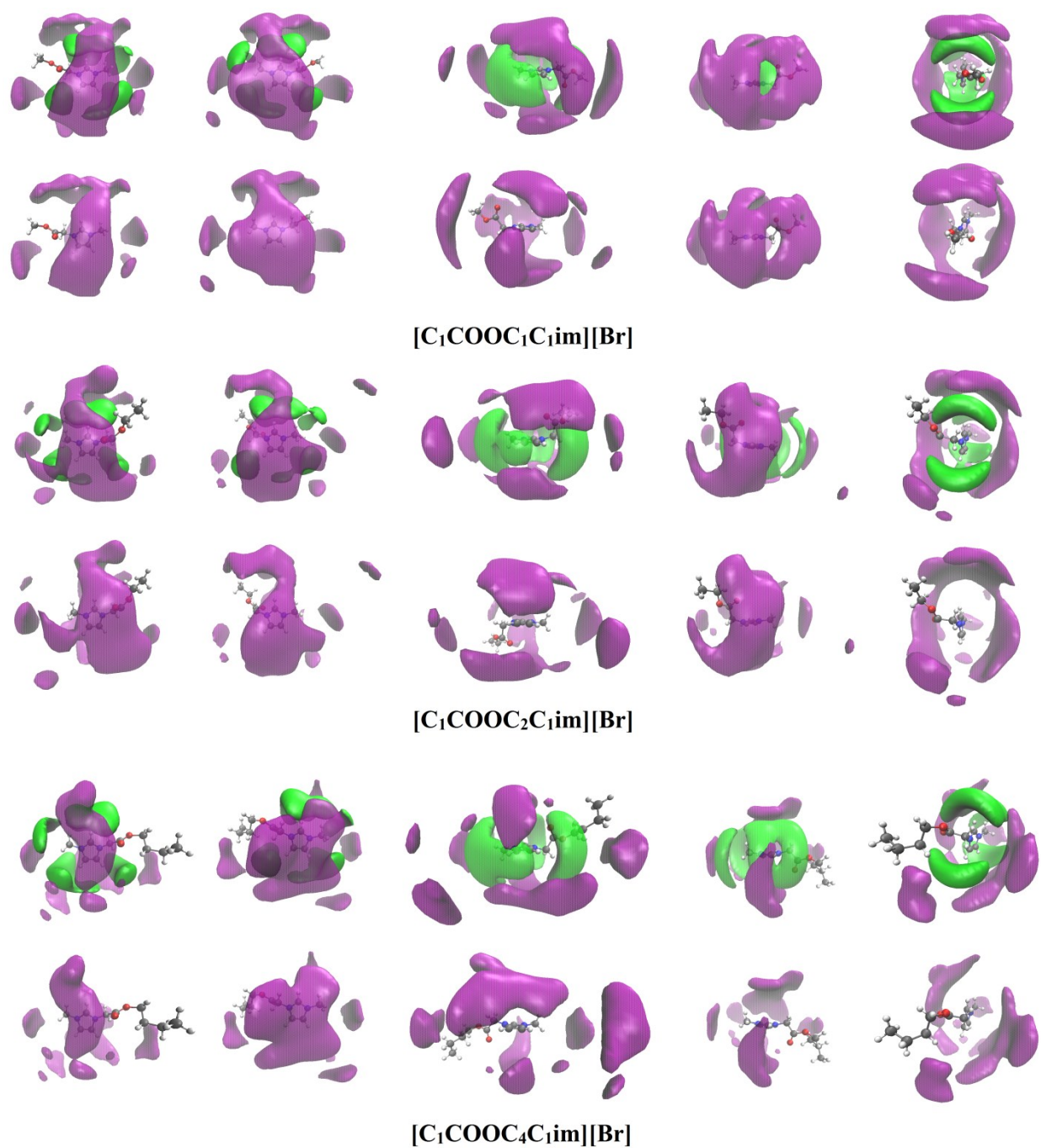
[C₁COOC₄C₁im][Br]

Figure S26. Cation-cation SDFs of neighbor cations around imidazolium ring of the reference cation for $[C_1COOC_nC_1im][Br]$ ILs at 400 K.

[C₁COOC₁C₁im][NO₃]

[C₁COOC₂C₁im][NO₃]
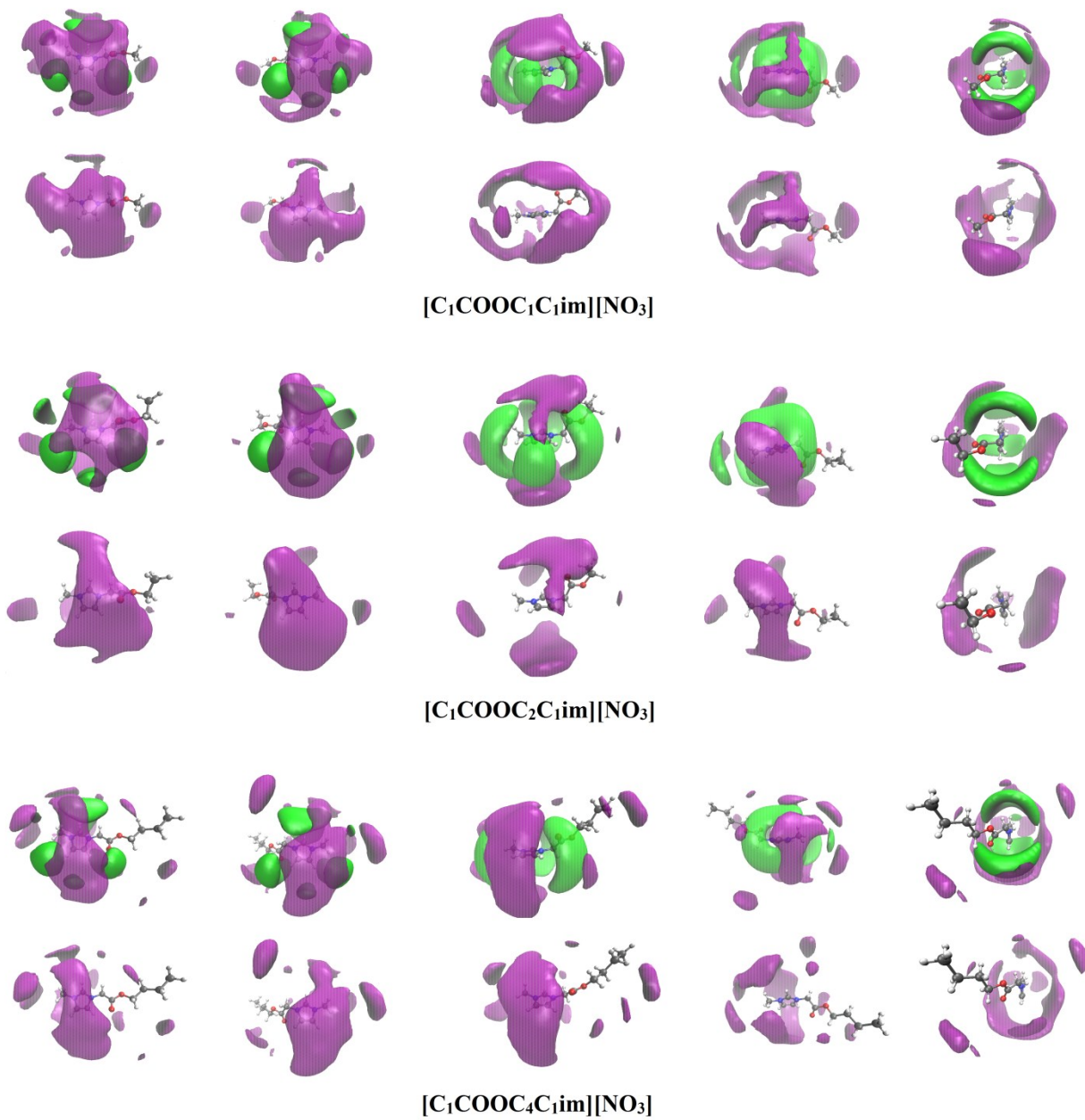
[C₁COOC₄C₁im][NO₃]

Figure S27. Cation-cation SDFs of neighbor cations around imidazolium ring of the reference cation for $[C_1COOC_nC_1im][NO_3]$ ILs at 400 K.

[C₁COOC₁C₁im][BF₄]

$[C_1COOC_1C_1im][BF_4]$

$[C_1COOC_2C_1im][BF_4]$
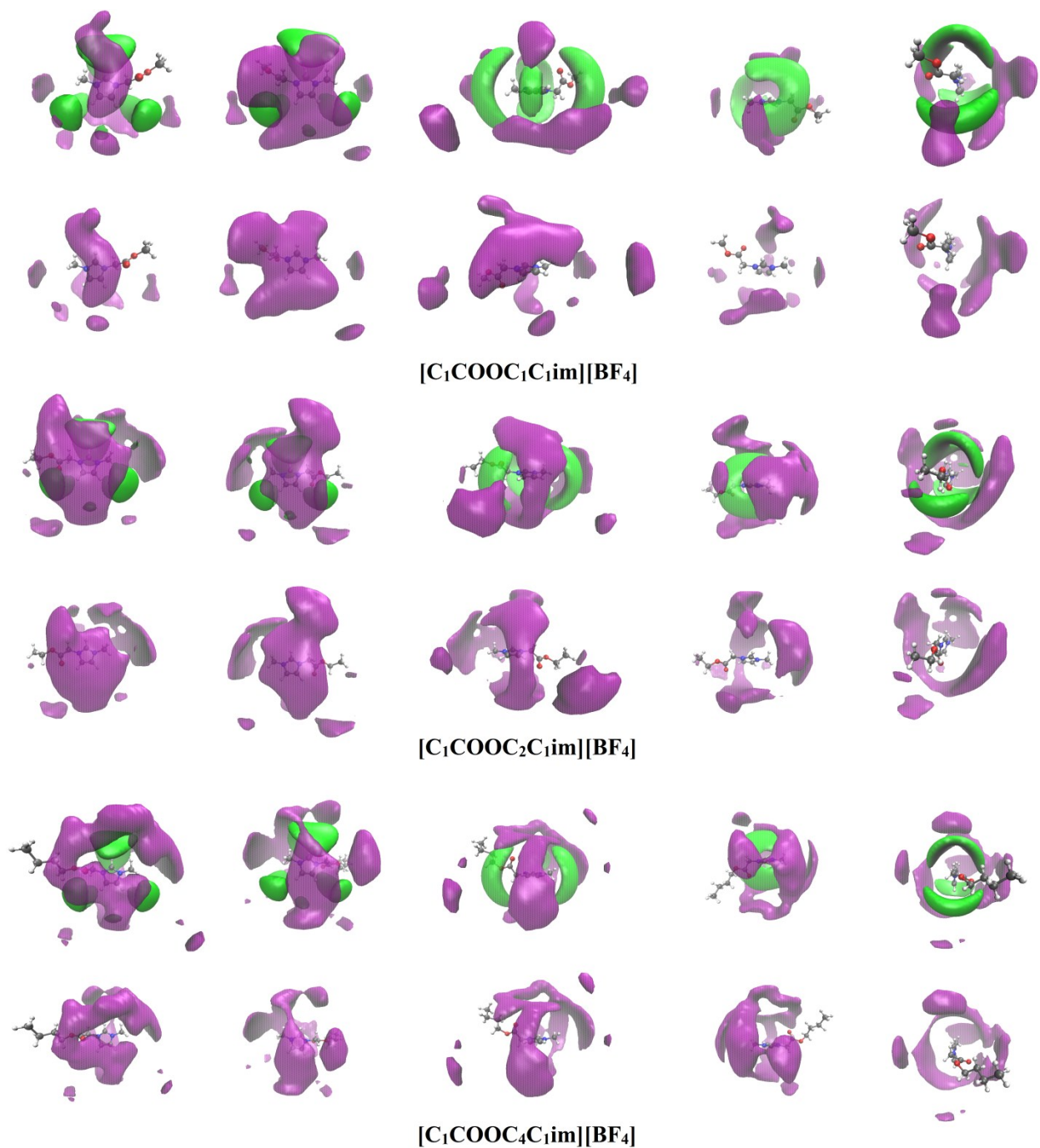
$[C_1COOC_4C_1im][BF_4]$

Figure S28. Cation-cation SDFs of neighbor cations around imidazolium ring of the reference cation for $[C_1COOC_nC_1im][BF_4]$ ILs at 400 K.

[C₁COOC₁C₁im][PF₆]

[C₁COOC₂C₁im][PF₆]
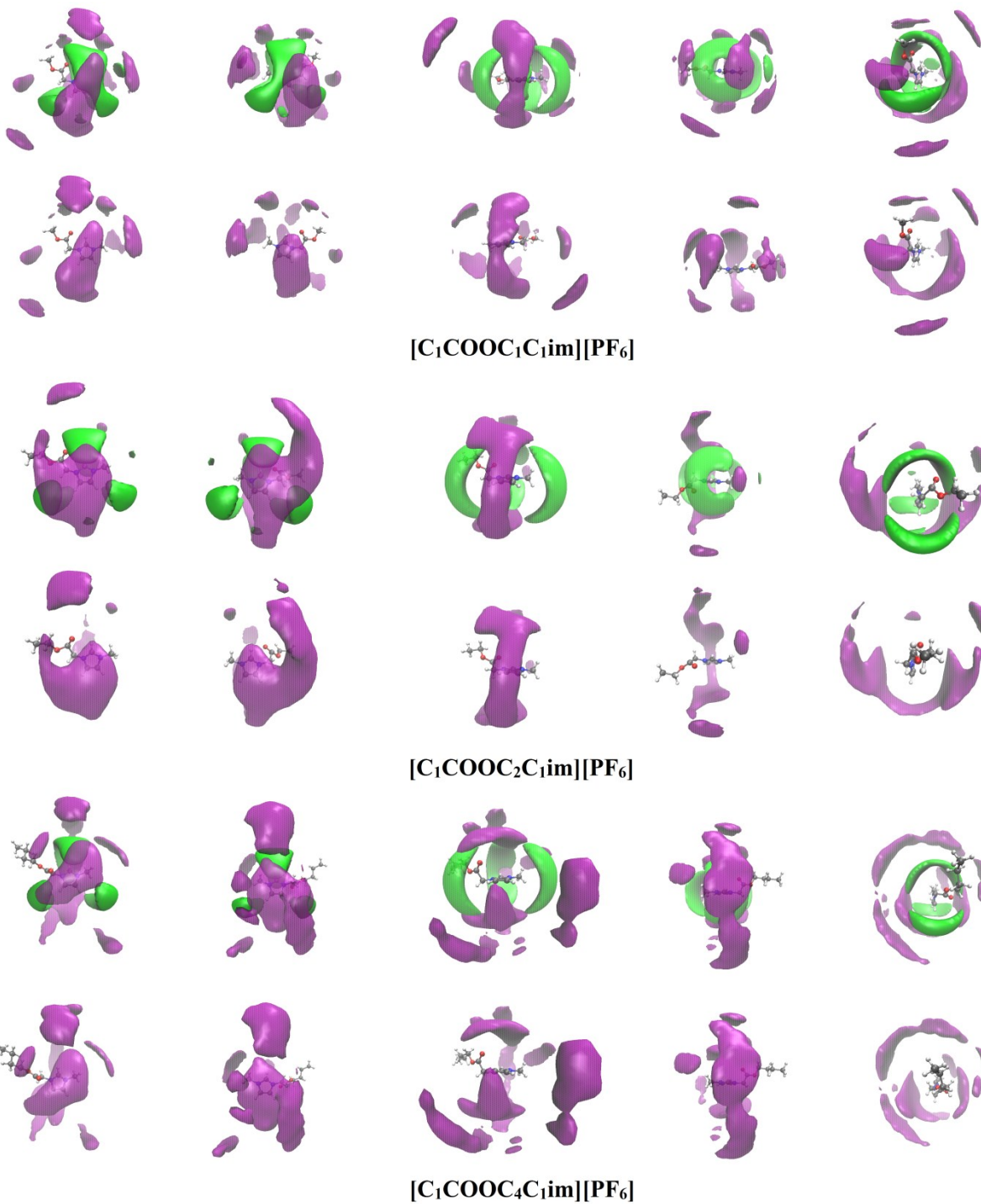
[C₁COOC₄C₁im][PF₆]

Figure S29. Cation-cation SDFs of neighbor cations around imidazolium ring of the reference cation for [C₁COOCₙC₁im][PF₆] ILs at 400 K.

[C₁COOC₁C₁im][TfO]

[C₁COOC₂C₁im][TfO]
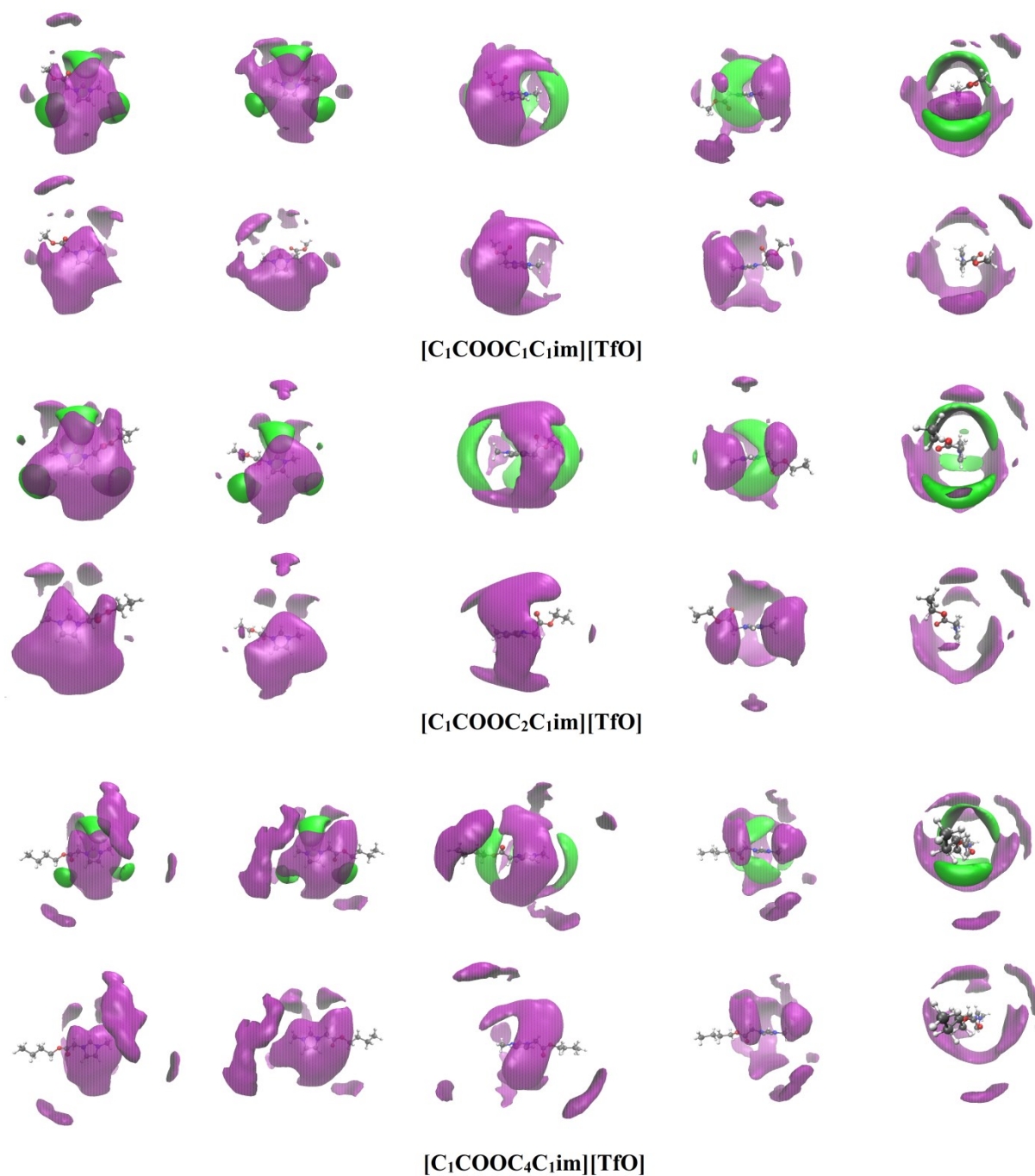
[C₁COOC₄C₁im][TfO]

Figure S30. Cation-cation SDFs of neighbor cations around imidazolium ring of the reference cation for [C₁COOC$_n$C₁im][TfO] ILs at 400 K.

Figure S31. Cation-cation SDFs of neighbor cations around imidazolium ring of the reference cation for $[C_1COOC_nC_1im][Tf_2N]$ ILs at 400 K.

[C_1COOC_1C_1im][Tf_2N]

[C_1COOC_2C_1im][Tf_2N]

[C_1COOC_4C_1im][Tf_2N]

References

(1)   C. J. Margulis, *Mol. Phys.*, 2004, **102**, 829-838.

(2)   Y. Wang, and G. A. Voth, *J. Am. Chem. Soc.*, 2005, **127**, 12192-12193.

(3)   J. N. A. Canongia Lopes and A. A. H. Pádua, *J. Phys. Chem. B*, 2006, **110**, 3330-3335.

(4)   A. A. H. Pádua, M. F. C. Gomes, J. N. A. Canongia Lopes, *Acc. Chem. Res.*, 2007, **40**, 1087-1096.

(5)   S. Tsuzuki, W. Shinoda, H. Saito, M. Mikami, H. Tokuda and M. Watanabe, *J. Phys. Chem. B*, 2009, **113**, 10641-10649.

(6)   K. Shimizu, A. A. H. Pádua and J. N. Canongia Lopes, *J. Phys. Chem. B*, 2010, **114**, 15635-15641.

(7)   T. Pott and P. Méléard, *Phys. Chem. Chem. Phys.*, 2009, **11**, 5469-5475.

(8)   T. L. Greaves, D. F. Kennedy, S. T. Mudie and C. J. Drummond, *J. Phys. Chem. B*, 2010, **114**, 10022-10031.

(9)   A. S. Pensado, A. A. H. Pádua and M. F. Costa Gomes, *J. Phys. Chem. B*, 2011, **115**, 3942-3948.

(10)   O. Russina, L. Gontrani, B. Fazio, D. Lombardo, A. Triolo and R. Caminiti, *Chem. Phys. Lett.*, 2010, **493**, 259-262.

(11)   O. Russina, A. Triolo, L.; Gontrani and R. Caminiti, *J. Phys. Chem. Lett.*, 2012, **3**, 27-33.

(12)   O. Russina, A. Triolo, L. Gontrani, R. Caminiti, D. Xiao, L. G. Hines, R. A. Bartsch, E. L. Quitevis, N. Plechkova and K. R. Seddon, *J. Phys.: Condens. Matter*, 2009, **21**, 424121-424129.

(13)   A. Triolo, O. Russina, H.-J. Bleif and E. Di Cola, *J. Phys. Chem. B*, 2007, **111**, 4641-4644.

(14)   A. Triolo, O. Russina, B. Fazio, R. Triolo and E. Di Cola, *Chem. Phys. Lett.*, 2008, **457**, 362-365.

(15)   X. Paredes, J. Fernández, A. A. H. Pádua, P. Malfreyt, F. Malberg, B. Kirchner and A. S. Pensado, *J. Phys. Chem. B*, 2012, **116**, 14159-14170.

(16)   S. Yeganegi, A. Soltanabadi and D. Farmanzadeh, *J. Phys. Chem. B*, 2012, **116**, 11517-11526.

(17)   Y. Shen, D. F. Kennedy, T. L. Greaves, A. Weerawardena, R. J. Mulder, N. Kirby, G. Song and C. J. Drummonda, *Phys. Chem. Chem. Phys.*, 2012, **14**, 7981-7992.

(18)   S. Li, G. Feng, J. L. Bañuelos, G. Rother, P. F. Fulvio, S. Dai and P. T. Cummings, *J. Phys. Chem. C*, 2013, **117**, 18251-18257.

(19)   A. A. Freitas, K. Shimizu and J. N. Canongia Lopes, *J. Chem. Eng. Data*, 2014, **59**, 3120-3129.

(20)   K. Shimizu, C. E. S. Bernardes and J. N. Canongia Lopes, *J. Phys. Chem. B*, 2014, **118**, 567-576.

(21)   K. Wei, L. Deng, Y. Wang, Z. Ou-Yang and G. Wang, *J. Phys. Chem. B*, 2014, **118**, 3642-3649.

(22)   R. Hayes, S. Imberti, G. G. Warr and R. Atkin, *J. Phys. Chem. C*, 2014, **118**, 13998-14008.

(23)   R. Hayes, G. G. Warr and R. Atkin, *Chem. Rev.*, 2015, **115**, 6357-6426.

(24)   J. N. Canongia Lopes, A. A. H. Pádua and K. Shimizu, *J. Phys. Chem. B*, 2008, **112**, 5039-5046.

(25)   W. Smith, T. R. Forester and I. T. Todorov, *the DL_POLY molecular simulation package, v. 2.18*, Daresbury Laboratory, UK, 2007.

(26)   M. J. Frisch, G. W. Trucks, H. B. Schlegel, G. E. Scuseria, M. A. Robb, J. R. Cheeseman, J. A. Montgomery, Jr. T. Vreven, K. N. Kudin, J. C. Burant, J. M. Millam, S. S. Iyengar, J. Tomasi, V. Barone, B. Mennucci, M. Cossi, G. Scalmani, N. Rega, G. A. Petersson, H. Nakatsuji, M. Hada, M. Ehara, K. Toyota, R. Fukuda, J. Hasegawa, M. Ishida, T. Nakajima, Y. Honda, O. Kitao, H. Nakai, M. Klene, X. Li, J. E. Knox, H. P. Hratchian, J. B. Cross, V. Bakken, C. Adamo, J. Jaramillo, R. Gomperts, R. E. Stratmann, O. Yazyev, A. J. Austin, R. Cammi, C. Pomelli, J. W. Ochterski, P. Y. Ayala, K. Morokuma, G. A. Voth, P. Salvador, J. J. Dannenberg, V. G. Zakrzewski, S. Dapprich, A. D. Daniels, M. C. Strain, O. Farkas, D. K. Malick, A. D. Rabuck, K. Raghavachari, J. B. Foresman, J. V. Ortiz, Q. Cui, A. G. Baboul, S. Clifford, J. Cioslowski, B. B. Stefanov, G. Liu, A. Liashenko, P. Piskorz, I. Komaromi, R. L. Martin, D. J. Fox, T. Keith, M. A. Al-Laham, C. Y. Peng, A. Nanayakkara, M. Challacombe, P. M. W. Gill, B. Johnson, W. Chen, M. W. Wong, C. Gonzalez and J. A. Pople, *Gaussian 03, Revision C.02*; Gaussian, Inc.: Wallingford, CT, 2004.

(27)   S. Nose´, *J. Chem. Phys.*, 1984, **81**, 511-519.

(28)   M. P. Allen and D. J. Tildesley, Computer Simulation of Liquids, Oxford Science Publications, Oxford, 1987.

(29)   K. D. Gibson and H. A. Scheraga, *J. Phys. Chem.*, 1995, **99**, 3752-3764.

(30)   M. Brehm and B. Kirchner, *J. Chem. Inf. Model.*, 2011, **51**, 2007-2023.